Original research article

Institution of MECHANICAL ENGINEERS
Journal of POWER AND ENERGY

Proc IMechE Part A:
J Power and Energy
2026, Vol. 0(0) 1–30

DOI: 10.1177/09576509261426237
journals.sagepub.com/home/pia
Sage

Performance enhancement of the triangular fins solar air heater by adding ribs on the side wall and middle section of absorber plate

Vineet Singh[1], Vinod Singh Yadav[2], Vaibhav Trivedi[1] and Pushkar Singh[2]

Abstract

This research article investigated the effect of the triangular fins and triangular fins with ribs by the ANSYS Fluent-2018. Ribs are added at the side walls of the solar air heater to divert the flow on the teethed portion of the absorber plate, which was hidden in previous research designed of the roughened solar air heater. The comparison between the two designs of the solar air heaters was done based on the thermal performance factor. The best design is selected and validated experimentally. The outcomes of the study showed that the triangular fins have a higher thermal performance factor than the triangular fins with the ribs due to lower pressure drop in the triangular fins. However, triangular fins have a lower Nusselt number as compared to triangular fins with ribs. The Reynolds Number and pitch to height ratio were chosen as important parameters which investigated the performance of the triangular fins solar air heater through numerically. The friction factor, Nusselt Number, and the Thermal Performance Factor (TPF) are reduced as the pitch to height ratio increases. The rise in Reynolds Number reduces the friction factor, but the Nusselt Number and TPF increase for a triangular fin solar air heater. The maximum value of the Nusselt Number and TPF obtained are 114.95 and 1.89 for the Reynolds Number 10,000 and P/h ratio of 1. The minimum friction factor reached 0.023 at a Reynolds Number of 10,000 and a P/h ratio of 3. The numerical results are validated with the experimental results on the date 11/03/2025. The maximum outlet temperature of air, thermal efficiency, and exergy obtained through the experimental observation are 72.25°C, 77.18%, and 3.4% at noon at a mass flow rate of 0.08 kg/s. The numerical results are validated with the experimental results within an accuracy of 5%.

Keywords

CFD, triangular fins, solar air heater, exergy, thermal performance factor

Introduction

The growing energy mandate is largely met by fossil fuels, but their high cost, environmental impact, and limited supply raise serious concerns. As a result, global research is focusing on renewable energy alternatives. Amid these, solar energy stands out for being abundant, clean, and cost-effective during daylight hours.[1,2] The primary benefit of solar energy compared to other energy sources is its cleanliness and minimal environmental footprint. The ever-increasing demand for energy to sustain developmental progress is primarily met by fossil fuels.[3] However, reliance on these sources raises concerns due to their escalating prices, finite reserves, environmental pollution, and non-renewable nature.[4,5] Although fossil fuels are the dominant energy source for the 20th century, thanks to their affordability and convenience, the environmental consequences were largely ignored until recently. Today, the environmental advantages of solar energy are becoming a central focus in energy planning and policy. Utilizing solar energy can significantly reduce global warming.[6] However, a major challenge remains in improving the efficiency of devices that convert solar energy into thermal energy.[7] Throughout history, solar energy has been used in countless ways by both nature and humans, from growing food to drying clothes. In modern times, it is deliberately harnessed for various applications, including heating commercial and domestic buildings, heating spaces for industrial and domestic purposes, powering swimming pool heaters, refrigerators, engines, and pumps, desalinating water, generating electricity, and more. With rising demand for thermal energy in residential and some industrial sectors, reliance on solar energy has become essential. A key factor in determining the practicality of solar energy over other sources is the efficiency of solar-to-thermal energy conversion devices. The efficiency depends on the system's ability to absorb solar irradiance, convert it into thermal energy, and transfer that thermal energy to a heat transfer (HT) medium with minimal losses.[8] Solar air heaters serve as solar-to-thermal energy conversion systems by capturing insolation and transforming it into heat, which is subsequently used to warm air for residential, agricultural, or industrial purposes. Their practicality largely depends on

[1]Department of Mechanical Engineering, School of Engineering & Technology, IFTM University, Moradabad, India
[2]Department of Mechanical Engineering, NIT Uttarakhand, Pauri, India

Corresponding author:
Vineet Singh, Department of Mechanical Engineering, School of Engineering & Technology, IFTM University, Moradabad 244102, India.
Email: vineetpsh@gmail.com

the efficiency of this energy conversion process, which is a critical factor when evaluating the competitiveness of solar energy against conventional sources.

Solar air heaters are systems designed to collect solar irradiance and transform it into thermal energy, thereby heating the air that flows over them. These systems provide a sustainable solution for applications that require low to medium temperature heat, such as space conditioning, indoor space heating, agricultural drying, and numerous industrial developments. Among the various solar air heater (SAH) configurations, triangular-finned designs have attracted significant care due to their potential to boost heat transfer performance.[9,10] Triangular fins, mounted on the absorber plate (AP), growth in exposed and active surface area for heat exchange with the flowing air, resulting in enhanced heat transfer rates compared to conventional flat plate collectors.[11] To validate both experimental and theoretical findings, Computational Fluid Dynamics (CFD) has been developed as a crucial tool for analysing and optimizing the performance of SAH. CFD simulations provide detailed perceptions into airflow patterns, temperature distributions, and HT characteristics within the system, enabling a comprehensive understanding of its thermal behaviour.[12,13] By regulating design parameters such as fin geometry, spacing, and airflow rates within the simulation environment, researchers can identify optimal configurations to maximize thermal efficiency. However, CFD models inherently involve assumptions and simplifications of real-world conditions, which may affect the accuracy and generalizability of the results. Therefore, experimental validation is crucial to ensure the authenticity and reproducibility of the CFD predictions. Experimental analysis of triangular finned SAHs involves constructing physical prototypes and measuring their performance under controlled conditions. Typically, these experiments involve measuring parameters such as outlet and inlet air temperatures, airflow rates, and solar irradiance intensity. By contrasting the experimental results with CFD predictions, researchers can validate the models and make refinements to enhance their accuracy. This integrated approach, combining CFD analysis with experimental validation, offers a robust framework for understanding the complex heat transfer mechanisms in triangular-finned solar air heaters and optimizing their design to improve performance.[14,15] This paper will further explore the intricacies of this combined approach and its implications for advancing SAH technology. A study addresses the low thermal efficiency of SAH due to poor HT between the solar air collector and air. To improve performance, triangular fins are added, and a numerical investigation is conducted using ANSYS Fluent 17.1 to compute turbulent flow dynamics. The study examines the impact of Re and fin height (varying from 0.93,845 to 16.104 mm) on performance, using an air flow rate of 0.001 to 0.011 kg/s.[10] The RNG k-ε turbulence model is validated and used for further investigation. This study experimentally analyses and optimizes a SAH with triangular fins arranged in random pattern. An experimental setup was developed at 28.10°N, 78.23°E, and HT through fins was evaluated using the Finite Difference Method. Response Surface Methodology in MINITAB-17 was used to optimize performance based on solar intensity (600–1000 W/m^2), Reynolds number (4000–6000), and fin base-to-height ratio (0.4–0.8). Key outputs analysed included outlet temperature, Nusselt number, and efficiencies. Optimal performance was achieved at 1000 W/m^2, Reynolds number (Re) 4969.7, and a fin ratio of 0.6060, yielding a thermal efficiency of 50.836% and exergy efficiency of 8.762%.[16] Research found that using spherical ribs on the absorber plate significantly enhanced thermohydraulic performance, with Nusselt numbers up to twice that of the base model with Re = 4000-25,000 and spherical rib diameter ranges from 0.5 to 2.5 cm.[17] The study emphases on enhancement of the performance of a triangular duct SAHs by incorporating a wavy fin on the solar air collector. An analytical model was developed using MATLAB to study the impact of fin pitch ratio (0.05–0.2) and fin amplitude ratio (0.025–0.125) on thermo-hydraulic efficiency (THE). Investigation reveals that increasing fin pitch ratio reduces efficiency, while increasing fin amplitude ratio improves it up to a critical Re. A highest thermal efficiency (TE) of 85% and THE of 80.16% were achieved. The maximum performance enhancement over a conventional design is 15.7%, and design plots assist in parameter selection.[18] CFD analysis of a SAH with arc-shaped ribs, conducted using ANSYS Fluent, employing the RNG k-ε turbulence model, reveals the best result on thermo-hydraulic performance (THP).[19] A CFD study of a SAH with a ribbed absorber plate analysed four turbulence models (RNG k-epsilon, standard k-ω, SST k-ω, and Realizable k-ε) over a Re range of 3000 - 15,000, focusing on Nusselt number, friction factor, and THP.[20] CFD and exergy analysis have been carried out, and results show that a V-shaped ribbed absorber in a triangular duct yields higher efficiency than in a rectangular duct.[21] An investigation using the SST k-ω turbulence model optimized a solar air heater through exergy analysis, achieving 1.81 times higher heat transfer and 3.13 times greater friction compared to a smooth duct, demonstrating that optimization enhances performance.[22]

Above, numerous CFD-based investigations, as presented in Table 1, concluded that SAHs with baffles, fins, and extended surfaces enhance thermal output; the k-ε RNG turbulence model showed good accuracy in predicting thermo-hydraulic performance (THP) of SAH. Lower pitch ratio and higher amplitude ratio significantly improve performance. Most of the studies emphasize geometry optimization and flow dynamics as critical to enhancing efficiency in solar air heaters. Wavy fins offer even higher performance, particularly with optimized pitch and amplitude ratios.

Research gap and novelty of the work

It has been observed through literature review on the solar air heater that fins and ribs combination significantly enhances the heat transfer and turbulence in the air flow path. The fins mainly increase the heat transfer by increasing the surface area of the absorber plate, and ribs work as the turbulator, mainly used to increase the turbulence of air. In all types of solar air heater, the length of the air flow path is around 1.5 m to 2.0 m, with which a maximum boundary layer thickness is 11 cm on one side. In this boundary layer region large amount of the air is accumulated near the side wall, and this region is dominated by the viscous flow. This region accounts 25% part of the solar air heater, which has the unheated air that will reduce the average temperature of

Table 1. Analytical, experimental and numerical investigation on finned-absorber plate SAHs.

Type of study	Type of heat absorbing plate/SAH	Type of duct/ channel/pass of SAH	Model/Approach description	Main/Notable findings
Theoretical and experimental[15]	Finned and flat plate absorber plate SAH	Rectangular channel SAH	• Iterative method implemented through MATLAB programming. • Fundamental energy balance model equations for each component of solar collector. • Correlation for thermo-hydraulic performance.	• Fin plate air collector efficiency is minimally affected by installation angle (only ~3% difference). • Efficiency varies notably with air mass flow, especially at low flow rates. • Placing the fan on top improves efficiency and temperature difference by about 5%, enhancing heat utilization.
Numerical and optimization (GE)[23]	Rectangular-shaped ribs on a flat plate absorber plate	Rectangular channel SAH	• Semi-empirical heat transfer model equations for thermo-hydraulic performance. • Performance optimization using genetic algorithm (GA). • The optimization focused on flow channel height, Re, rib relative height, and relative pitch.	• The optimal rib pitch ratio and rib height ratio for a SAH are 10 and 0.025, respectively, across a wide range of flow conditions. • The optimum L/H ratio increases while the W/H ratio decreases with increase in temperature difference. The optimal channel height and Re remain relatively stable, while rib height and spacing can be somewhat interchanged.
Experimental[9]	Four type absorber plate: •Flat plate AP • Double triangular fins AP (inline paired i.e. dual triangular fins AP, staggered dual triangular fins AP, inclined staggered dual triangular fins AP)	Rectangular channel SAH	• Energy and exergy evaluation combined with economic and environmental analysis were performed as part of this study.	• The system outperformed a flat plate AP in efficiency and energy output, while reducing CO_2 emissions by up to 14.3 tons. • The finned AP consistently showed a higher temperature difference than that of flat plate AP across all tested mass flow rates (MFRs).
Theoretical and experimental[14]	Triangular shaped long channel on flat plate absorber plate	Triangular duct/ channel SAH	Reversing (U-shaped air circulating pattern)	• The presented solar air heater achieves the same efficiency with less surface area than a flat plate collector. • Under constant MFR and typical conditions, the U-turn triangular channel SAH required 25% less surface area than that of a simple flat plate SAH. • The optimal thermohydraulic performance occurred at a 60° internal peak angle within the 35–120° range.
Numerical and theoretical method (CFD)[24]	• V-shaped ribs • Artificial roughness	Rectangular channel SAH	• CFD models: k-ε RNG turbulent model, k-ε RZ model, k-ε SST model, k-ε standard model compared with empirical relation. • The discrete ordination method is employed to track the direction and strength of solar radiation. • Angle of attack (α) = 30°-60°, e/D = 0.02 to 0.04, P/e = 10, Re = 2,500-18,000. • Solar flux = 1000 W/m^2.	• The investigation shows $(\eta_{eff})_{max}$ = 74% at Re = 14000 and at constant e/D = 0.034. • Friction factor decreases.

(continued)

Table 1. (continued)

Type of study	Type of heat absorbing plate/SAH	Type of duct/ channel/pass of SAH	Model/Approach description	Main/Notable findings
Numerical method (CFD)[25]	• Transverse ribs with a square wave pattern. • Irregular rib. • Unvarying cross-sectioned rib.	Rectangular channel SAH	• RNG k-ε turbulent model. • P/e = 4-30, Re = 3,000-15,000, fixed e/D = 0.043	• The optimum values of 'Nu' and 'f' were found to be 2.14 and 3.55 times more than those of a smooth duct, respectively, at P/e = 10 and Re = 15,000. • The THP of the irregular rib was found to be superior to that of the unvarying cross-sectioned rib. • Maximum THP parameter was found to be 1.43 at P/e = 10 and Re = 12,000.
Numerical method (CFD)[26]	• Finned absorber plate. • Different fin angle.	Rectangular channel double pass (DP) SAH.	All CFD turbulence models were used to compare the results.	• Optimized THP and designed parameters were obtained for DP-SAH for the RNG k-ε turbulent model.

the air. To solve this issue, this research article used triangular staggered fins, having the ribs at the side wall of the solar air heater, for diverting the unheated air accumulated near the side walls of the SAH. This design of the SAH is novel and new and has not been reported in previous research. This study aimed to enhance the THP of a SAH equipped with a triangular-finned solar air collector or absorber plate with ribs and to compare the computational results obtained through ANSYS Fluent with corresponding experimental data.

Numerical investigation

The numerical investigation of the SAH with triangular fins and triangular fins with ribs has been done by ANSYS Fluent 2018. The fluent software mainly handles the air flow and heat transfer problem by visualizing the flow field through the velocity, pressure, and temperature distribution without experimental analysis. These governing model equations are used to visualise the flow field. These equations represent the conservation of momentum, mass and energy in form of the partial derivatives.[27]

➢ Conservation of mass equation.[28,29]

$$\frac{\partial(\rho u)}{\partial x}+\frac{\partial(\rho v)}{\partial y}+\frac{\partial(\rho w)}{\partial z}=0 \tag{1}$$

➢ Momentum equation.[30]

• X- Momentum equation

$$\rho\left(\frac{u\partial u}{\partial x}+\frac{v\partial u}{\partial y}+\frac{w\partial u}{\partial z}\right) = \rho g_x-\frac{\partial P}{\partial x}+\frac{\partial}{\partial x}\left(\frac{2\mu\partial u}{\partial x}+\lambda\vec{\nabla}.\vec{V}\right) + \frac{\partial}{\partial y}\left[\mu\left(\frac{\partial u}{\partial y}+\frac{\partial v}{\partial x}\right)\right]+\frac{\partial}{\partial z}\left[\mu\left(\frac{\partial u}{\partial z}+\frac{\partial w}{\partial x}\right)\right] \tag{2}$$

• Y- Momentum equation

$$\rho\left(\frac{u\partial v}{\partial x}+\frac{v\partial v}{\partial y}+\frac{w\partial v}{\partial z}\right) = \rho g_y-\frac{\partial P}{\partial y}+\frac{\partial}{\partial x}\left[\mu\left(\frac{\partial v}{\partial x}+\frac{\partial u}{\partial y}\right)\right] + \frac{\partial}{\partial y}\left[2\mu\left(\frac{\partial y}{\partial y}+\lambda\overrightarrow{\nabla.\vec{V}}\right)\right]+\frac{\partial}{\partial z}\left[\mu\left(\frac{\partial v}{\partial z}+\frac{\partial w}{\partial y}\right)\right] \tag{3}$$

• Z- Momentum equation

$$\rho\left(\frac{u\partial w}{\partial x}+\frac{v\partial w}{\partial y}+\frac{w\partial w}{\partial z}\right) = \rho g_z-\frac{\partial P}{\partial z}+\frac{\partial}{\partial x}\left[\mu\left(\frac{\partial w}{\partial x}+\frac{\partial u}{\partial z}\right)\right] + \frac{\partial}{\partial y}\left[\mu\left(\frac{\partial v}{\partial z}+\frac{\partial w}{\partial y}\right)\right]+\frac{\partial}{\partial z}\left[\frac{2\mu\partial w}{\partial z}+\lambda\overrightarrow{\nabla.\vec{V}}\right] \tag{4}$$

Energy equation[31]

$$\rho C_P\left(\frac{u\partial T}{\partial x}+\frac{v\partial T}{\partial y}+\frac{w\partial T}{\partial Z}\right)=\beta T\left(\frac{u\partial P}{\partial x}+\frac{v\partial P}{\partial y}+\frac{w\partial P}{\partial z}\right) + \overrightarrow{\nabla.(k\overrightarrow{\nabla T})}+\phi \tag{5}$$

Here, u, v, and w represent the air velocities components in the x, y and z directions, respectively and the β is the coefficient of volume expansion. The term ϕ is known as viscous dissipation. It is denoted by the equation given by.[22]

Turbulence model

There are several models (Laminar, Inviscid, Transition SST, k-omega, Scale Adaptive Simulation (SAS), Reynolds Stress, Detached Eddy Simulation (DES), k-epsilon, and large eddy simulation) available, which can be used for determining the flow characteristics in CFD. The selection

of the model has been done based on the accuracy of the results. In this SAH model analysis k-ε (two equation) model has been used for determining the velocity and pressure distribution with good accuracy.[22]

K-ε model

In the k-ε turbulence model, the 'k' denotes the turbulent kinetic energy (KE), while 'ε' denotes the rate of dissipation of turbulent KE, both of which characterize the turbulence within the system.

The velocity and length scale are defined in terms of 'k' and 'ε' by the following equation.[32]

$$v = k^{\frac{1}{2}}, \tag{6}$$

$$l = \frac{k^{\frac{3}{2}}}{\varepsilon} \tag{7}$$

So, the following are the two equations representing in terms of k and ε.[32]

$$\frac{\partial(\rho k)}{\partial(t)} + div(\rho k U) = div\left[\frac{\mu_t}{\sigma_t} gradk\right] + 2\mu_t S_{ij}.S_{ij} - \rho\varepsilon \tag{8}$$

$$\frac{\partial(\rho\varepsilon)}{\partial(t)} + div(\rho\varepsilon U) = div\left[\frac{\mu_t}{\sigma_\varepsilon} gradk\right] + C_{1\varepsilon}\left(\frac{\varepsilon}{k}\right)2\mu_t S_{ij}.S_{ij} - \frac{C_{2\varepsilon}\rho\varepsilon^2}{k} \tag{9}$$

Where μ_t represents the eddy viscosity by the following equations

$$\mu_t = \frac{\rho C_\mu k^2}{\varepsilon} \tag{10}$$

The value of 5 constants used in the above equation is represented below.[32]

$$\sigma_\varepsilon = 1.30, C_\mu = 0.09, \sigma_K = 1.00, C_{1\varepsilon} = 1.44\, and\, C_{2\varepsilon} = 1.92 \tag{11}$$

Boundary conditions

Figure 1 illustrates the SAH with various boundary conditions. In the simulation, the SAH is divided into two zones: the first is the fluid zone, and the second is the solid zone. The fluid and solid zones are made of air and copper material. The properties of the air and copper are given in Table 2. The interface boundary conditions are applied at the interface of the solid and liquid surfaces. The properties of the fluid at the inlet and outlet portions are considered as uniform. The inlet velocity and temperature are given to the inlet fluid at inlet boundary conditions, the outlet pressure is applied at the outlet pressure boundary conditions. The side walls of the solar air heater (SAH) are modelled as adiabatic walls. The Roseland solar radiation model is used to calculate the solar flux on a particular day and time of the year.

Figure 2 illustrates the steps for conducting the analysis using ANSYS Fluent 2018. Initially, both designs of the Triangular Fins Solar Air Heater (TFSAH) and Triangular Fins Solar Air Heater with Ribs (TFSAHR) are drawn in the Fluent Designer Modeller at the same dimensions. In the next step, the meshing of both designs is completed, and the quality is checked for good accuracy of the results. Furthermore, the naming of the parts is done, and apply the boundary conditions to run the simulation. In the next step, check the convergence of the simulation and determine the temperature, velocity, and pressure field to calculate the values of the various responses numerically.

Figure 3 represents the pictorial view of the design model geometry, meshing, and the mesh quality. Figure 3(a) displays the picture of the absorber plate with the triangular fins, in which the fins are soldered on the 2 mm-thick copper plate. Figure 3(b) represents the complete 3D picture of the SAH, in which the side walls are considered adiabatic, and the upper glass is considered transparent with an absorptivity of 4%. Figure 3(c) represents the meshing on the SAH. The total nodes and the number of meshing elements to be considered are 345,120 and 1817537. The number of meshes is selected based on the calibration of the orthogonality, skewness, aspect ratio, and the grid independence

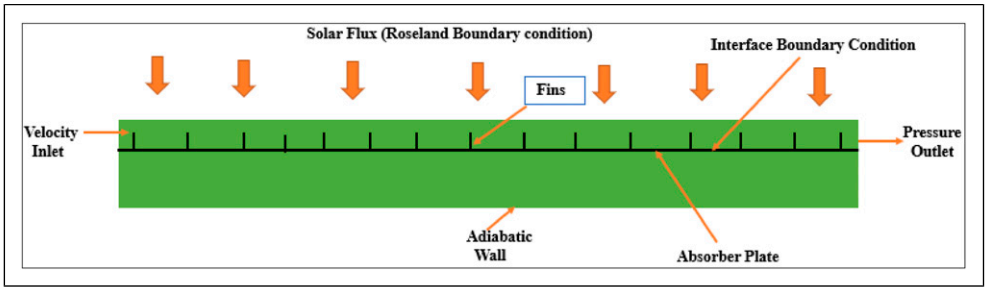

Figure 1. Schematic diagram of the boundary conditions on the SAH.

Table 2. Material properties of the air and the copper.[33]

Material	Density (kg/m^3)	Specific heat (KJ/kg K)	Dynamic viscosity (kg/m-s)	Thermal conductivity (W/m K)
Air	1.225	1.006	0.000017894	0.0242
Copper	8978	0.381	-	387.6

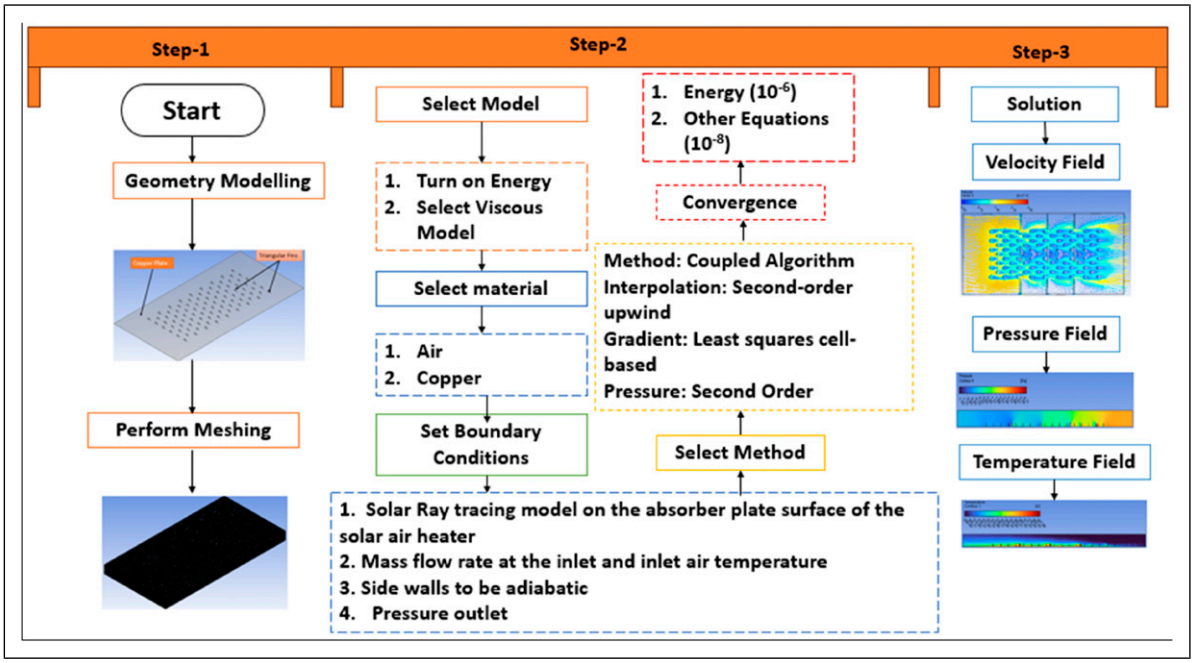

Figure 2. Steps followed in simulation.

test. Figure 3(d) represents the orthogonality of the meshing, the orthogonality measures how close the angle between the adjacent to 90°. Closing the value of the orthogonality to 1 represents the ideal mesh. The figure indicates that the maximum value of orthogonality is 0.9964 and the average value of orthogonality is 0.78, which signifies the best quality of the mesh.

Figure 3(e) illustrates the skewness of the meshes since skewness signifies the shape of the mesh element with the ideal shape, like an equilateral. The lower value of the skewness represents the best mesh quality,[34] and a higher value of the skewness gives the worst mesh quality. The average value of the skewness is 0.22, which represents the best quality of the meshes. Figure 3(f) demonstrates the aspect ratio of the meshes, which is the ratio of the longest side to the shortest side, higher values of the aspect ratio, the average value of the aspect ratio is 1.18, which signifies the highest quality of the mesh.[35]

Figure 3(g) displays the graphical representation of the grid independence test which shows the 'Nu' variation with the number of elements. The figure indicates that as the number of elements rises from the 2.375×10^5 to 1.81×10^6, the Nusselt number increases from 92.85 to 99.91 which shows the growth of 76% but if the number of elements rise further to 1.95×10^6 then increase in Nusselt number 1.11%. So, for the reduction of computational expense/cost, the selected number of mesh elements count is 1.81×10^6 at the level of good accuracy.

Energy analysis of the solar air heater

Figure 4 depicts the HT among the AP, glass, air, and the atmosphere. Figure 4(a) shows the energy interaction among the AP to the atmosphere, glass and the flowing air. The solar flux reaching the AP enhanced its temperature. The higher temperature of the AP transfers the energy to the glass, air, and atmosphere through radiation and convection. So, apply the solar and thermal energy balance to the solar air collector (SAC) or AP.

Solar Energy received by absorber plate = Energy supplied to the glass by radiation + convection heat transfers to the air + energy transfer to the atmosphere.[36]

$$S^*A_{Ab} = U_t A_{Ab}(T_{ab} - T_{atm}) + h_{air}A_{Ab}(T_{ab} - T_{air}) + \frac{\sigma A_{ab}\left(T_{ab}^4 - T_g^4\right)}{\left(\frac{1}{\varepsilon_{ab}}\right) + \left(\frac{1}{\varepsilon_g}\right) - 1} \tag{12}$$

$$S = U_t(T_{ab} - T_{atm}) + h_{air}(T_{ab} - T_{air}) + \frac{\sigma\left(T_{ab}^4 - T_g^4\right)}{\left(\frac{1}{\varepsilon_{ab}}\right) + \left(\frac{1}{\varepsilon_g}\right) - 1} \tag{13}$$

Where S is the solar flux, T_{ab} is the temperature of the absorber plate, T_{atm} is the temperature of the atmosphere, T_{air} is the air average temperature, σ is the Stefan-Boltzmann constant, ε_{ab} and ε_g are the emissivity of the absorber plate and the glass, and U_t is the overall heat transfer coefficient (HTC). The h_{air} is the HTC from the absorber plate.

Energy balance for the toughened glass by the AP as presented in Figure 4(b).

Energy transfer by absorber plate to toughened glass by mode of radiation = Energy transfer by glass to atmosphere + Energy transfer by glass to air.[37]

$$\frac{\sigma A_{ab}\left(T_{ab}^4 - T_g^4\right)}{\left(\frac{1}{\varepsilon_{ab}}\right) + \left(\frac{1}{\varepsilon_g}\right) - 1} = h_{ga}A_{ab}\left(T_g - T_{air}\right) + h_{gatm}A_{ab}\left(T_g - T_{atm}\right) \tag{14}$$

$$\frac{\sigma\left(T_{ab}^4 - T_g^4\right)}{\left(\frac{1}{\varepsilon_{ab}}\right) + \left(\frac{1}{\varepsilon_g}\right) - 1} = h_{ga}\left(T_g - T_{air}\right) + h_{gatm}\left(T_g - T_{atm}\right) \tag{15}$$

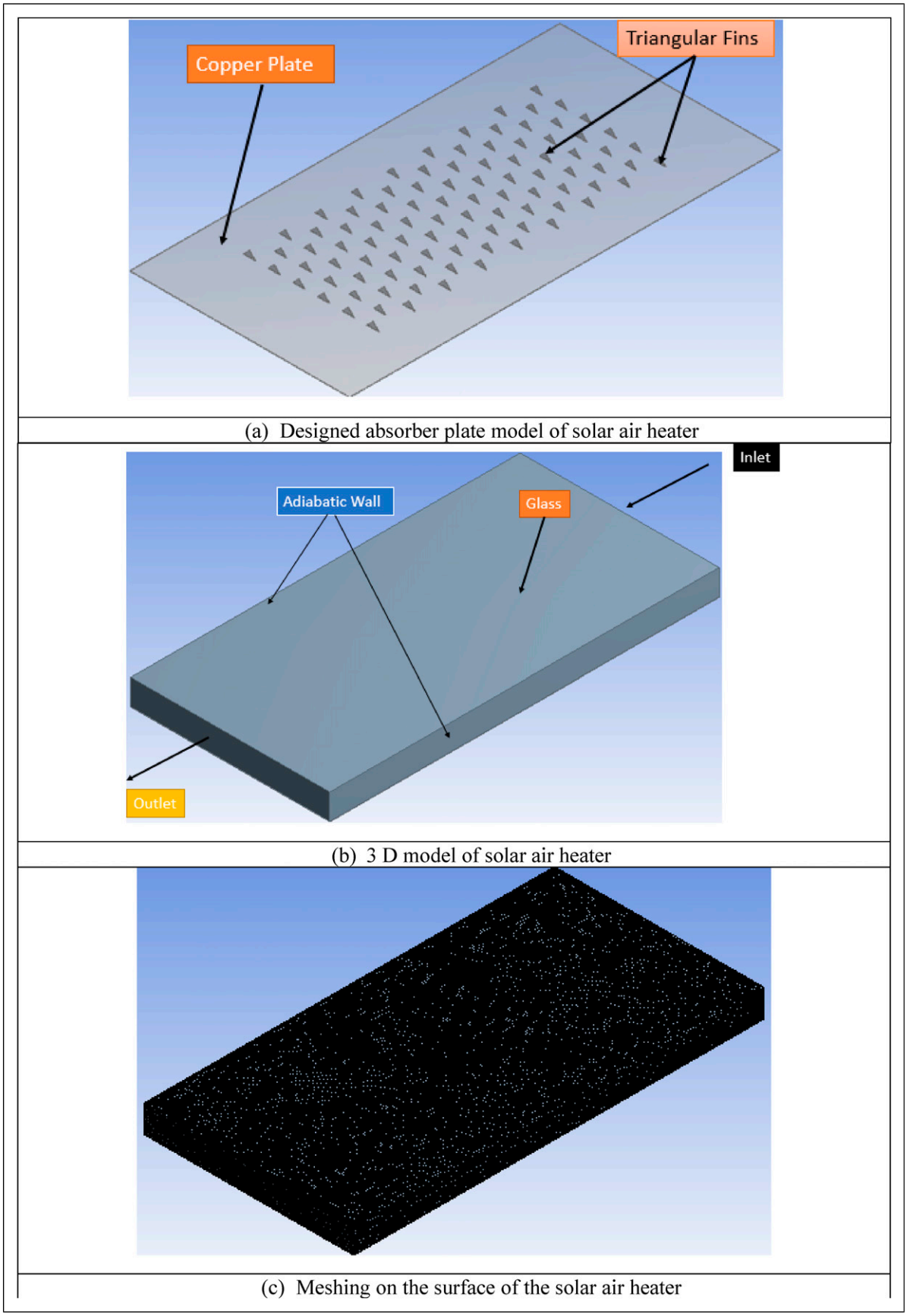

Figure 3. Geometry and meshing on the solar air heater.

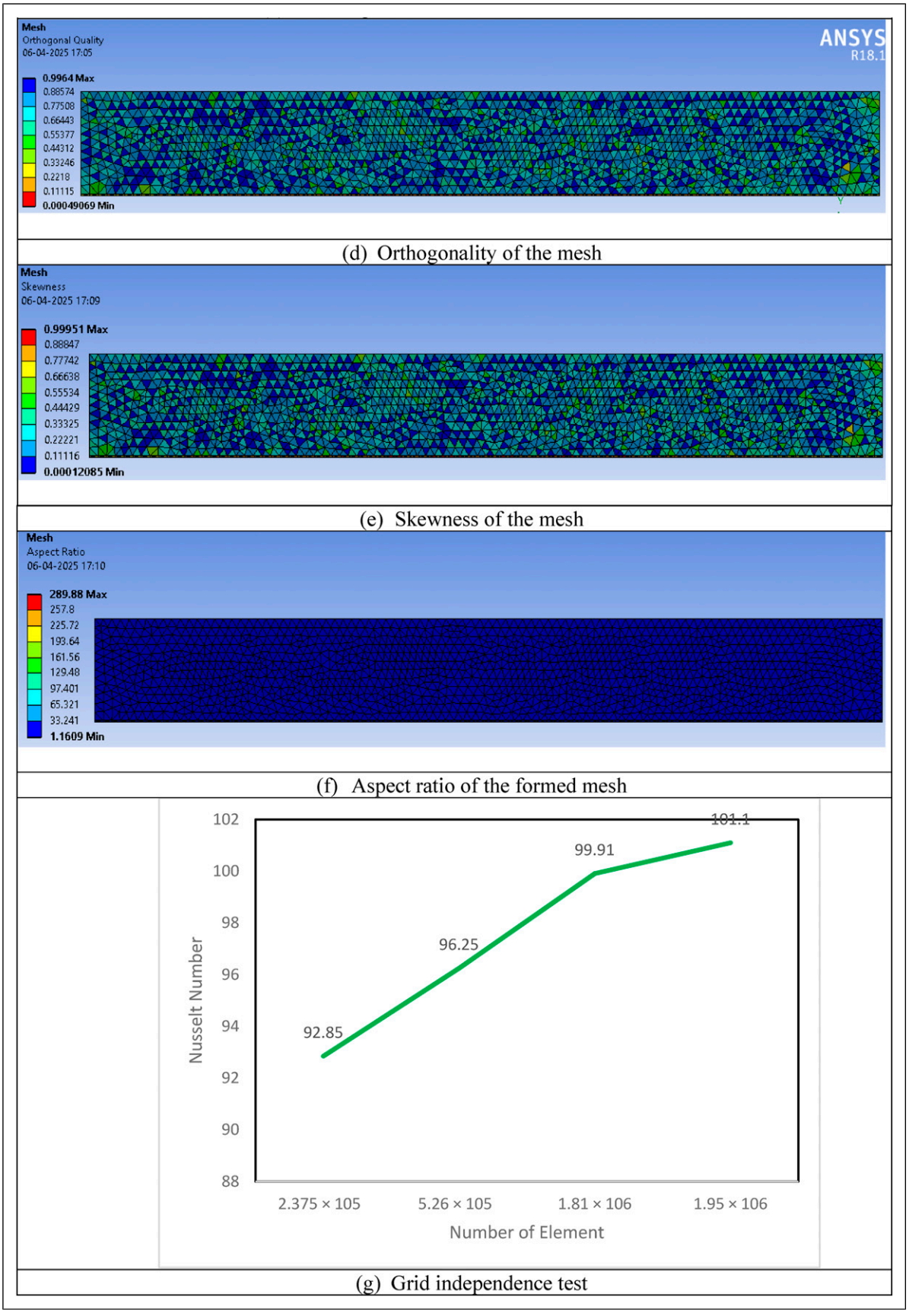

Figure 3. Continued.

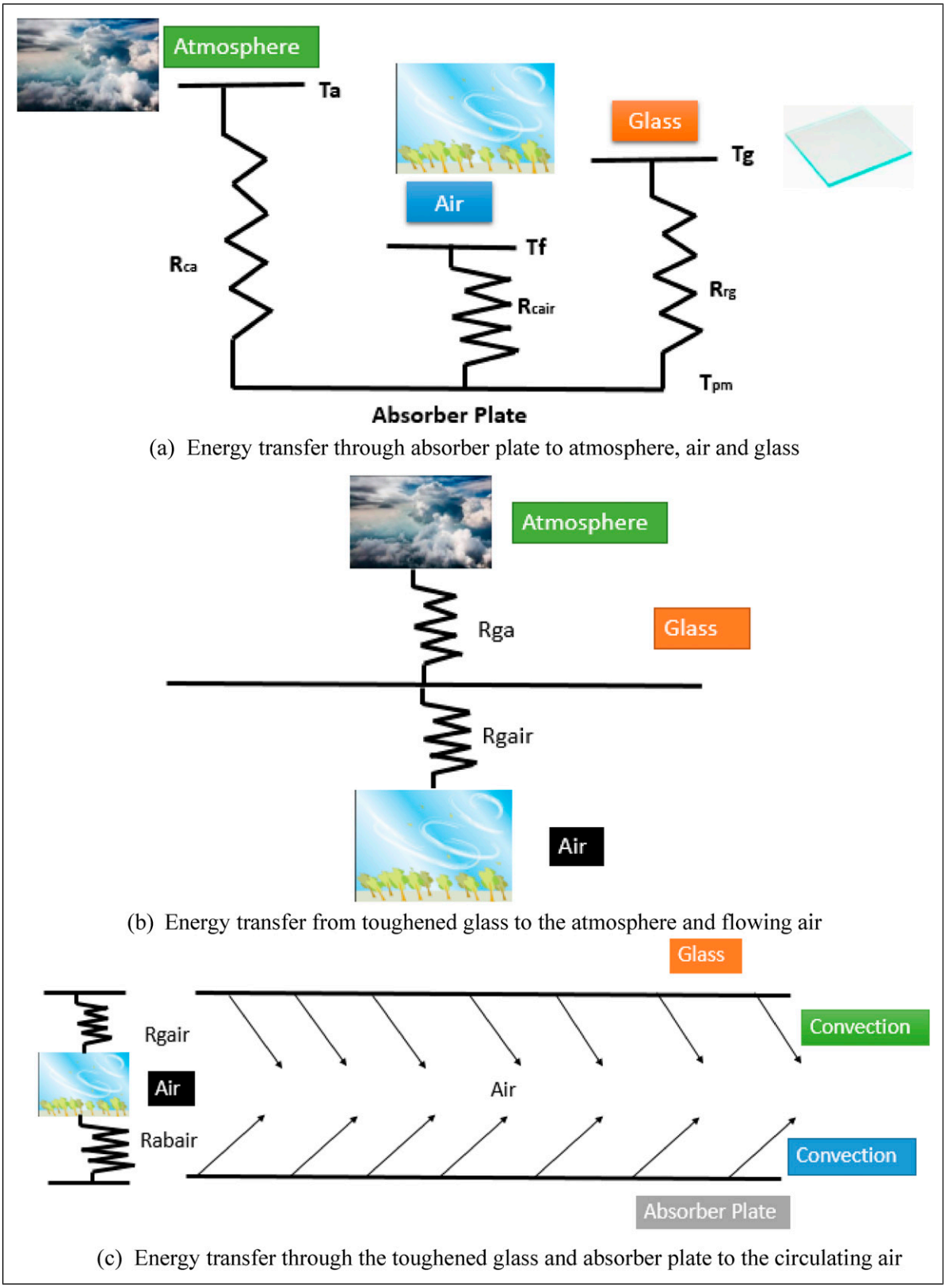

Figure 4. Energy transfer within the solar air heater by both convection and radiation inside the SAH.

h_{ga} and h_{gatm} are the HTC of glass to air and glass to the atmosphere.

The HT to the air occurs through the AP and the glass Figure 4(c).[38,39]

$$m_{air}C_P(T_2 - T_1) = h_{ga}A_{ab}(T_g - T_{air}) + h_{aba}(T_{ab} - T_{air}) \quad (16)$$

Here, C_P is the specific heat of the air, m_{air} represents the mass flow rate (MFR) of the air, T_1 and T_2 are the inlet and outlet temperature of air.

If the surface of the SAH is considered to be smooth, then the Nusselt number (Nu) and friction factor (f) are determined by the correlations.[39,40]

$$Nu = 0.0158Re^{0.8} \quad (17)$$

$$f = 0.079Re^{-0.25} \tag{18}$$

The 'Nu' and 'f' on a finned surface are determined by knowing the HT rate and pressure drop experimentally.[41]

The HTC of glass to the atmosphere is calculated as Ref. 42

$$h_w = 5.7 + 3.8V \tag{19}$$

Where 'V' is the velocity of air above the glass of SAH.

The HT to the air is calculated by the following formula[43]

$$Q = m_{air}C_P(T_2 - T_1) \tag{20}$$

This heat gain of air occurs due to the transfer of heat by convection mode from the AP to the flowing air.

So, the HTC of the finned surface is determined by the equation[44,45]

$$h_{aba} = \frac{m_{air}C_P(T_2 - T_1)}{A_{ab}(T_{ab} - T_{mair})} \tag{21}$$

Furthermore, the Nusselt number is calculated as Ref. 46

$$Nu = \frac{h_{aba}D_e}{k_{air}} \tag{22}$$

Where De is the equivalent diameter, calculated by the following relation.

$$D_e = \frac{4A_c}{P} \tag{23}$$

The friction factor is calculated by the pressure drop with the equation.[43]

$$f = \frac{\Delta P D_e}{2LV^2\rho_a} \tag{24}$$

Where 'V' is the velocity of air inside the SAH, 'ΔP' is the pressure drop (PD), 'L' is the length of the SAH, and ρ_a is the density of air at the mean fluid temperature.

As the roughness over the surface of the AP increases, the pressure drops and HT both increase, which enhances the blower power significantly. So, a relative measure must be calculated, which determines the enhancement of HT as compared to the pressure drop. The Thermo-hydraulic performance (THP) must be evaluated as expressed in the following equation.[43]

$$THP = \frac{\frac{Nu_f}{Nu_s}}{\left(\frac{f_f}{f_S}\right)^{\frac{1}{3}}} \tag{25}$$

The thermal efficiency is defined as "the ratio of the actual heat transferred to the air to the total solar energy received by the SAH".[47]

$$\eta_{Th} = \frac{m_{air}C_P(T_2 - T_1)}{S^*A_{ab}} \tag{26}$$

Fin analysis

The surface area of the triangular fins is calculated as represented in Figure 5.[39]

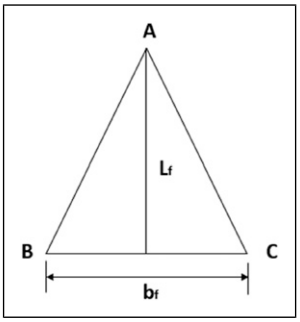

Figure 5. Fin design.

$$A_{Tf} = N_f\left(\frac{1}{2}b_f L_f\right)^* t_f \tag{27}$$

Where L_f is the fin height, A_{Tf} is the total surface area of the fins, N_f is the number of fins, b_f is the fin base, and t_f is the fin's thickness.

The fin efficiency for the triangular fins is given by Ref. 48.

$$\eta = \left(\frac{1}{mL_f}\right)\left(\frac{I_1(2mL_f)}{I_0(2mL_f)}\right) \tag{28}$$

The following equation calculates the m

$$m = \sqrt{\frac{2h}{kb_f}} \tag{29}$$

I_1 is the Bessel function of the Ist kind and Ist order, while I_0 is the Bessel function of the first kind and zero order.

The following equation calculates the actual HTC of the fins.

$$Q_{fin} = N\eta h_{aba}A_{fin}(T_{ab} - T_{air}) \tag{30}$$

Where N is the number of the fins, h_{aba} is the HTC of the absorber plate to air, A_{fin} is the area of the fin and T_{ab} is the temperature of the absorber plate, and T_{air} is the mean temperature of the air.

The fin effectiveness is calculated by Ref. 49.

$$\varepsilon_{fin} = \eta\left(\frac{A_{fin}}{A_b}\right) \tag{31}$$

A_{fin} is the area of the fin, and A_b is the area of the fin base. The Base area of the fin is computed by equation (32).

$$A_b = b_f t_f \tag{32}$$

Put these values in the above equation.[50]

$$\varepsilon_{fin} = \eta\left(\frac{L_f}{2}\right) \tag{33}$$

The effectiveness of the fins shows the benefits of adding the extended surface on the AP.

Exergy assessment of the solar air heater

The exergy analysis considered the real performance analysis. It explores the possibility of the extent to which the limit system will benefit or incur a loss. The SAH is the open

thermodynamic system in which cold air enters from the inlet and the heated air coming out from the outlet of the SAH. The various form of energy interaction occurs with the SAH in the form of heat and work as presented in Figure 6.

The exergy balance equation is applied to the SAH system.[51]

$$\frac{dE_{XCV}}{dt} = -\left(1-\frac{T_a}{T_p}\right)Q_{Loss} + E_{XSun} - \left(1-\frac{T_a}{T_g}\right)Q_r + W + m_{air}\left(e_{f1}-e_{f2}\right) \quad (34)$$

For the steady flow process, the equation can be written as Ref. 52.

$$E_{XSun} + W = m_{air}\left(e_{f2}-e_{f1}\right) + \left(1-\frac{T_a}{T_p}\right)Q_{Loss} + \left(1-\left(\frac{T_a}{T_g}\right)\right)Q_r \quad (35)$$

The left-hand side term represents the exergy supplied to the SAH. it has two terms, the 1st term denotes the Sun's exergy, and the 2nd term denotes the electric work supplied to the blower. The sun exergy represented by following equation.[48]

$$E_{XSun} = AS\left[1-\left(\frac{4}{3}\right)\left(\frac{T_a}{T_{Sun}}\right)+\left(\frac{1}{3}\right)\left(\frac{T_a}{T_{Sun}}\right)^4\right] \quad (36)$$

In equation (34), the right-hand side first term denotes the thermal exergy recovered due to heating of the cold air. The second part in right-hand side denotes the exergy loss due to the losses in the atmosphere due to temperature and reflection.

The exergetic efficiency is defined as "the ratio of the exergy recovered, and input exergy supplied".[28]

$$\eta_X = \frac{m_{air}\left(e_{f2}-e_{f1}\right)}{E_{Xsun}+W} \quad (37)$$

$$\text{The } m_{air}\left(e_{f2}-e_{f1}\right) = m_{air}\left[C_p\left((T_2-T_1)-T_O\ln\left(\frac{T_2}{T_1}\right)\right) + RT_O\ln\left(\frac{P_2}{P_1}\right)\right] \quad (38)$$

Put these values in the above equation, then exergy efficiency (EE) is expressed as given in Ref. 53.

$$\eta_X = \left(m_{air}\left[C_p\left((T_2-T_1)-T_O\ln\left(\frac{T_2}{T_1}\right)\right) + RT_O\ln\left(\frac{P_2}{P_1}\right)\right]\right) \Big/ \left(AS\left[1-\left(\frac{4}{3}\right)\left(\frac{T_a}{T_{Sun}}\right) + \left(\frac{1}{3}\right)\left(\frac{T_a}{T_{Sun}}\right)^4\right] + W\right) \quad (39)$$

The above equation shows that the EE depends on the outlet air temperature, solar irradiance, MFR, and ambient temperature.

Experimental setup

Figure 7 represents the experimental setup of the triangular fins SAH. It has 94 triangular fins in an irregular pattern on the absorber plate, which have a height and width of 25.4 mm and 50 mm, respectively. The pitch of the fins, which is the distance between the centre of the fins, is 9 cm. The solar air heater's dimensions are 180 cm in length, 70 cm in width, and 15 cm in thickness. The air flow passage height is measured to be 8 cm; this is an important parameter used to find the value of the Re calculation. The blower is used to flow the air through the inlet, and a digital anemometer is used to record the velocity of air at the inlet region.

The pyrometer measures the solar flux reaching the surface of the SAH. The thermocouples are fixed over the AP surface of the SAH at the top (point 3), middle (point 4), and bottom (point 5) sections for calculating the average temperature of the AP. The air temperature of the inlet (point 1) and outlet sections (point 2) is also measured using thermocouples. Three thermocouples, numbered 6, 7, and 8, were used to measure the temperature of the fin base, middle, and top, which helps determine the temperature distribution across the fin's length, as presented in Figure 8. The micromanometer is used to record the PD along the length of the SAH. Finally, thermocouples are connected with the monitor display to record the temperature at various points.

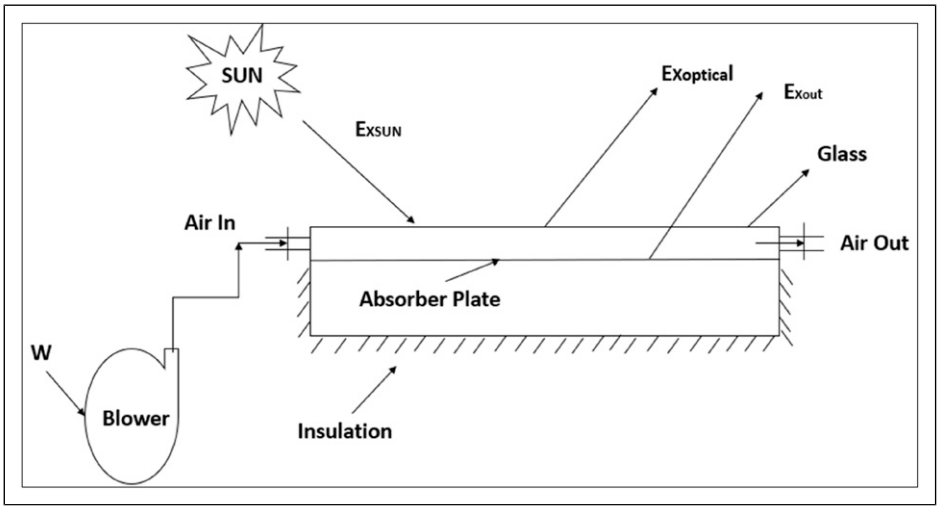

Figure 6. Exergy interaction with the solar air heater.

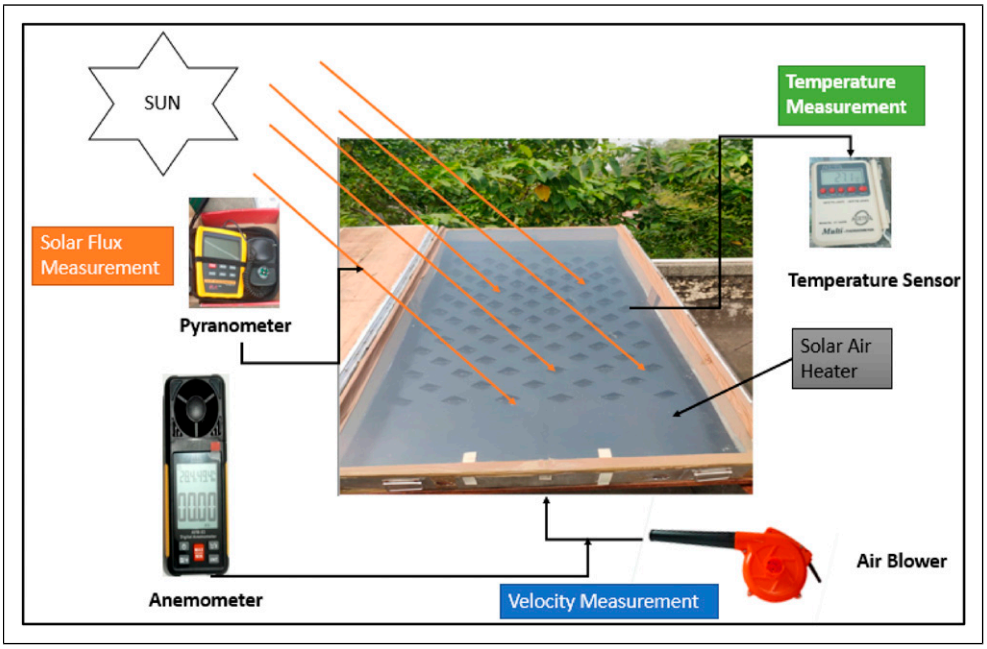

Figure 7. Pictorial view of the experimental setup.

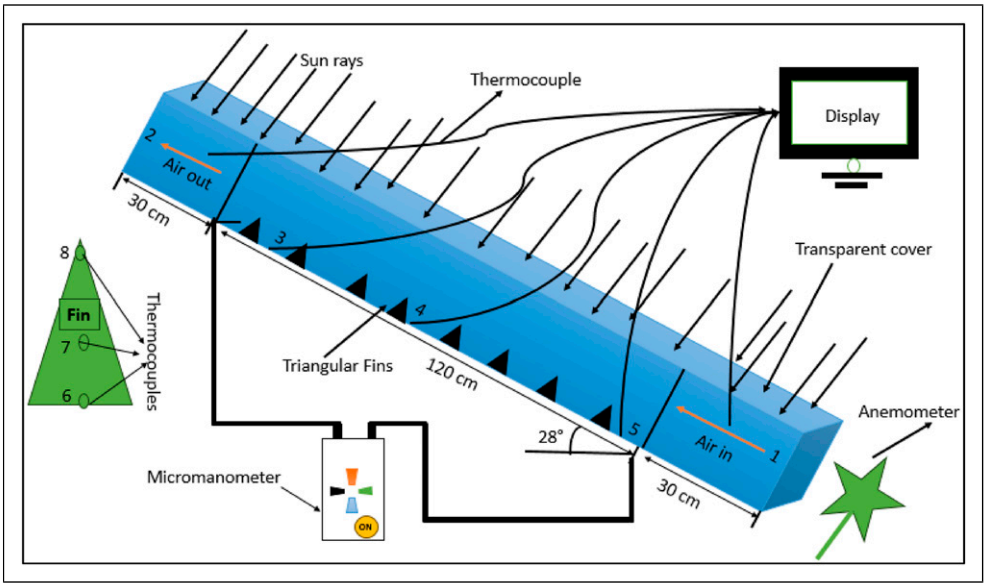

Figure 8. Visual picture of the Experimental setup.

The experimental data is collected at the optimum inclination of the SAH; the inclination angle provided is 28°. To increase the accuracy of the experimental data, the instruments have been checked for calibration. A total of 30 samples of experimental data were collected from 9 a.m. to 6 p.m. on three consecutive days of March 11–13, 2024. The three consecutive days of the month have been selected to increase the precision of the experimental runs. Furthermore, the final data has been determined by taking the average of the three consecutive days. Before starting to collect the experimental data, the experimental setup started at 8.30 a.m. so that the system would reach in steady state at 9.00 a.m. The main purpose of the experiments, collect sufficient data that determined the performance of the SAH in terms of the thermal efficiency, Nusselt Number, pressure drop, TPF, and exergy efficiency. For that inlet, outlet temperature, average temperature of the absorber plate, and pressure drop have been determined at a constant mass flow rate. Moreover, the performance variation of the SAH was also tested at varying mass flow rates.

Uncertainty analysis

It determines and quantifies the variability of the responses in the experimental observations due to the variation of the input variables. The measurement always has some error, which is reflected in the responses. The uncertainty calculation can be used in risk analysis to determine the error in the system. The subsequent equations are used to compute the uncertainty in the responses. The uncertainty in the SAH efficiency is calculated as per the method represented in Ref. 54,55

The inlet and outlet temperatures of air were recorded using thermocouples with an accuracy of ±1.15%, while the inlet air velocity was recorded using a digital anemometer with an accuracy of ±1%. The mass flow rate (MFR) was determined based on the recorded inlet air velocity. The PD was recorded using a micromanometer with an accuracy of ±1.9%, while solar intensity was recorded using a digital pyranometer or solar power meter with an accuracy of ±2.10%. The overall uncertainty in the instruments and responses is represented by Tables 3 and 4.

Economic analysis

SAH indeed reduces the environmental pollution, but it should be economical since the product will be used by the public. The manufacturing cost, running cost, and maintenance are such that it will be used in the agriculture sector, in which farmers are the end users. In this section, the total cost of the SAH is determined, which includes the cost of the components, energy consumption and the manufacturing cost. Table 4 represents the cost of the various components used in the SAH which is depends on the number of the factor since the money value is changed in the future.

The annual cost of the SAH is depends on the life of the SAH and the inflation rate. So, the annual cost (AC) of the solar air heater is given by following equation.[57]

$$AC = TC*\frac{i(1+i)^n}{(1+i)^n - 1} \tag{40}$$

The Annual maintenance cost (AMC) is 10% of the AC, which includes the repair cost of the instruments.

The Annul salvage value (ASV) of the component is the cost of the scrap, which must be deducted from the total cost.[58]

Table 3. Uncertainty in the responses and input variables.

S. No.	Parameter	Instruments used	Uncertainty
1.	Temperature	Thermocouples	1.15%
2.	Solar intensity	Pyranometer	2.10%
3.	Velocity	Digital anemometer	1%
4.	Pressure	Micro-manometer	1.90%

$$ASV = S_L.\frac{i}{(1+i)^n - 1} \tag{41}$$

The salvage value is the 20% of the total cost of the product.[59]

$$S_L = 0.2TC \tag{42}$$

The Uniform Annual Cost (UAC) is represented by the following relation.[60]

$$UAC = AC + AMC + APC - ASV \tag{43}$$

APC represents the Annual Power Cost of the SAH, which depends on the mass flow rate of the air passes over the surface of the solar air heater.

Table 5 represents the cost of the various components of the solar air heater. The sum of all components of the SAH represents the initial investment. Table 6 shows the annual cost, annual maintenance cost, annual salvage cost, annual earnings through the heating of the air, and the annual profit through the SAH. The total earnings can be achieved through the SAH by reducing the electricity consumption for heating the air. The total earnings through the SAH can be done 101.06 $ which will be a good source of earnings for the poor farmers.

Results and discussion

CFD analysis results

Velocity vector plots. Figure 9 represents the velocity vector plot to know the air particle movement over the surface of the SAH. Figure 9(a) and (b) display the picture of the velocity vector plot of the TFSAH and TFSAHR at the inlet air velocity of 2.0 m/s. Figure 9(a) indicates that a lot of air is accumulated near the side walls of the SAH, which will reduce the turbulence and remain unheated, reducing the average outlet air temperature but due to staggered fashion of the triangular fins on absorber plate, the lot of turbulence in middle section of the plate. The air is attached at the side walls of the SAH due to no slip boundary conditions.

Figure 9(b) shows that adding the ribs on the side wall and the middle portion of the absorber plate diverts the wall air on the finned section of the absorber plate, which will increase the turbulence and the average outlet air temperature. However, adding ribs also enhanced the pressure drop

Table 4. Uncertainty calculation.[56]

Parameter	Formula	Uncertainty formula	Uncertainty
Density	$\rho = \frac{P}{RT}$	$\frac{\partial\rho}{\rho} = \sqrt{\left(\frac{\partial P}{P}\right)^2 + \left(\frac{\partial T}{T}\right)^2}$	$\sqrt{(1.90)^2 + (1.15)^2} = 2.22\%$
Mass flow rate	$m = \rho AV$	$\frac{\partial m}{m} = \sqrt{\left(\frac{\partial \rho}{\rho}\right)^2 + \left(\frac{\partial V}{V}\right)^2}$	$\sqrt{(2.22)^2 + (1)^2} = 2.43\%$
Useful heat gain	$Q_u = m_{air}C_P(T_2 - T_1)$	$\frac{\Delta Q_u}{Q_u} = \sqrt{\left(\frac{\Delta m_{air}}{m_{air}}\right)^2 + 2\left(\frac{\Delta T}{T}\right)^2}$	$\sqrt{(2.43)^2 + 2*(1.15)^2} = 2.92\%$
Heat transfer coefficient	$h = \frac{Q_u}{A_P(T_P - T_a)}$	$\frac{\partial h}{h} = \sqrt{\left(\frac{\partial Q_u}{Q_u}\right)^2 + 2\left(\frac{\partial T}{T}\right)^2}$	$\sqrt{(2.92)^2 + 2*(1.15)^2} = 3.34\%$
Nusselt number	$Nu = \frac{hD_h}{k}$	$\frac{\partial Nu}{Nu} = \frac{\partial h}{h}$	3.34%
Thermal efficiency	$\eta_{th} = \frac{m_{air}C_p(T_2 - T_1)}{SA_{ab}}$	$\frac{\Delta\eta_{th}}{\eta_{th}} = \sqrt{\left(\frac{\Delta m_{air}}{m_{air}}\right)^2 + 2\left(\frac{\Delta T}{T}\right)^2 + \left(\frac{\Delta S}{S}\right)^2}$	$= \sqrt{(2.43)^2 + 2(1.15)^2 + (2.10)^2} = 3.6\%$

over the surface of the absorber plate. Now similar vector plot is also presented in Figure 9(c) and (d) at the inlet air velocities of 2.5 m/s and 1.0 m/s. Due to higher turbulence on the surface of absorber plate, the maximum velocity of the air is higher than the inlet air velocity.

Figure 9(e) illustrates the velocity vector plot of the SAH in the Y-Z direction, which depicts high turbulence of the flowing air inside the SAH box above the fins and around the fins' surface. Figure shows the higher circulation in between the teethed section of the absorber plate. It will increase the travelling time of the air from inlet to outlet that will increase the heat transfer and Nusslet Number but simultaneously also increased the friction factor and blower power.

Pressure drops inside the SAH. Figure 10 represents the pressure variation in TFSAH and TFSAHR at different inlet air velocities. The total pressure drop is the sum of the skin friction drag and the form drag. The skin friction drag is mainly contributed by surface texture and air viscosity, and form drag is due to the fins' triangular shape. The front side of the triangular shape represents the maximum pressure, and the rear side contributes the low pressure. The maximum pressure in TFSAH (Figure 10(a)) and TFSAHR (Figure 10(b)) is 2.70 Pa and 4.11 Pa, respectively, at the inlet air velocity of 2.0 m/s. The addition of ribs at the side walls of the SAH enhances the PD as shown in Figure 10(b), which depicts, the ribs enhance HT as well as PD. As the inlet air velocity increases, the pressure rises proportionally to the square of the velocity. If the inlet air velocity increases to 2.5 m/s, the pressure drop enhances and reaches 6.40 Pa. The ribs are beneficial for the solar air heater if their net effect is to increase the HT rate. So, a Thermal Performance Factor (TPF) has been defined, which measures the relative performance of the HT and pressure drop as represented by equation (25).

Temperature variation at different sections of the SAH. Figure 11 depicts the temperature distribution profile in the solar air heater in both models, TFSAH and TFSAHR. The solar ray tracing model has been used to define the location and month of the year in the model as 11 March 2025, time 12 p.m. Based on the results, Figure 11(a)–(d) show the temperature distribution in the TFSAH and TFSAHR, respectively, at various times of the day. Figure 11(a) and (b) depict the maximum temperatures of TFSAH and TFSAHR, which are 381.45 K and 387.96 K, respectively, indicating that the temperature is maximum in TFSAHR. The addition of the ribs enhances the outlet air temperature but increases the turbulence and intense mixing of the air. A similar pattern is also seen in Figure 11(c) and (d) at 11 a.m. and 10 a.m. on 11 March 2025.

Table 5. Various components cost of SAH.

Material	Cost ($)
Top glass cover	12.15
Blower	26.12
Frame	52.45
Absorber plate	93
Insulator	1.85
Construction cost	67.1
Power consumptions	24.14
Total cost	276.81

Comparison of TFSAH and TFSAHR

Pressure drop. Figure 12 illustrates the PD in the TFSAH and TFSAHR, which shows that as the MFR increases, the pressure drops (PD) increases. The TFSAHR always has a higher PD than the TFSAH due to extra ribs inserted in the flow path of the air. These ribs create the turbulence and mixing in the flow path. The PD on the surface of the AP is directly proportional to the square of the airflow velocity (Form Drag) and the friction factor between the air and the AP. The pressure drop on the TFSAHR enhances the friction factor and form drag.

Thermal performance factor. Figure 13 represents the Thermal Performance Factor (TPF) variation with the 'Re'. The TPF is an important factor that determines the thermohydraulic performance of the SAH. The TPF values decided that the roughened surface enhances the HT or consumes more energy by increasing the friction factor. It is indicated that the thermal performance factor will increase as the 'Re' increases. The comparative results of the TFSAH and TFSAHR depict that as the Re increases, the TPF of the TFSAH is higher than the TFSAHR if the 'Re' rises above 6000. The lower than 6000 Reynolds Number TPF of the TFSAHR is higher than the TFSAH. The Lower TPF values of the TFSAHR are because to the higher pressure drop by the ribs as compared to the rise in Nusselt Number (Nu). Furthermore, the numerical and experimental results have been validated with the Gupta et al. (1997),[61] Momin et al. (2002),[62] and Sahu et al. (2022) (Arc-shaped apex).[63]

The present study of the TFSAH and TFSAHR of numerical and experimental findings shows a similar pattern as presented by Sahu et al. (2022), Gupta et al. (1997), and Momin et al. (2002). Moreover, after increasing the Reynolds number from 14,000, the curve becomes flattened and takes a downward trend since further increase in Reynolds Number reduced the useful heat gain with enhanced pressure drop. It has also been noted in both experimental and numerical studies that the temperature drop is continuously reduced with the Reynolds Number, but due to an

Table 6. Annual cost of the SAH and profit.

TC ($)	AC ($)	AC ($)	S ($)	ASV ($)	AMC ($)	UAC ($)	Annual earnings ($)	Total profit ($)
276.81	15	30.38	55.362	2.20	3.038	46.218	147.28	101.06

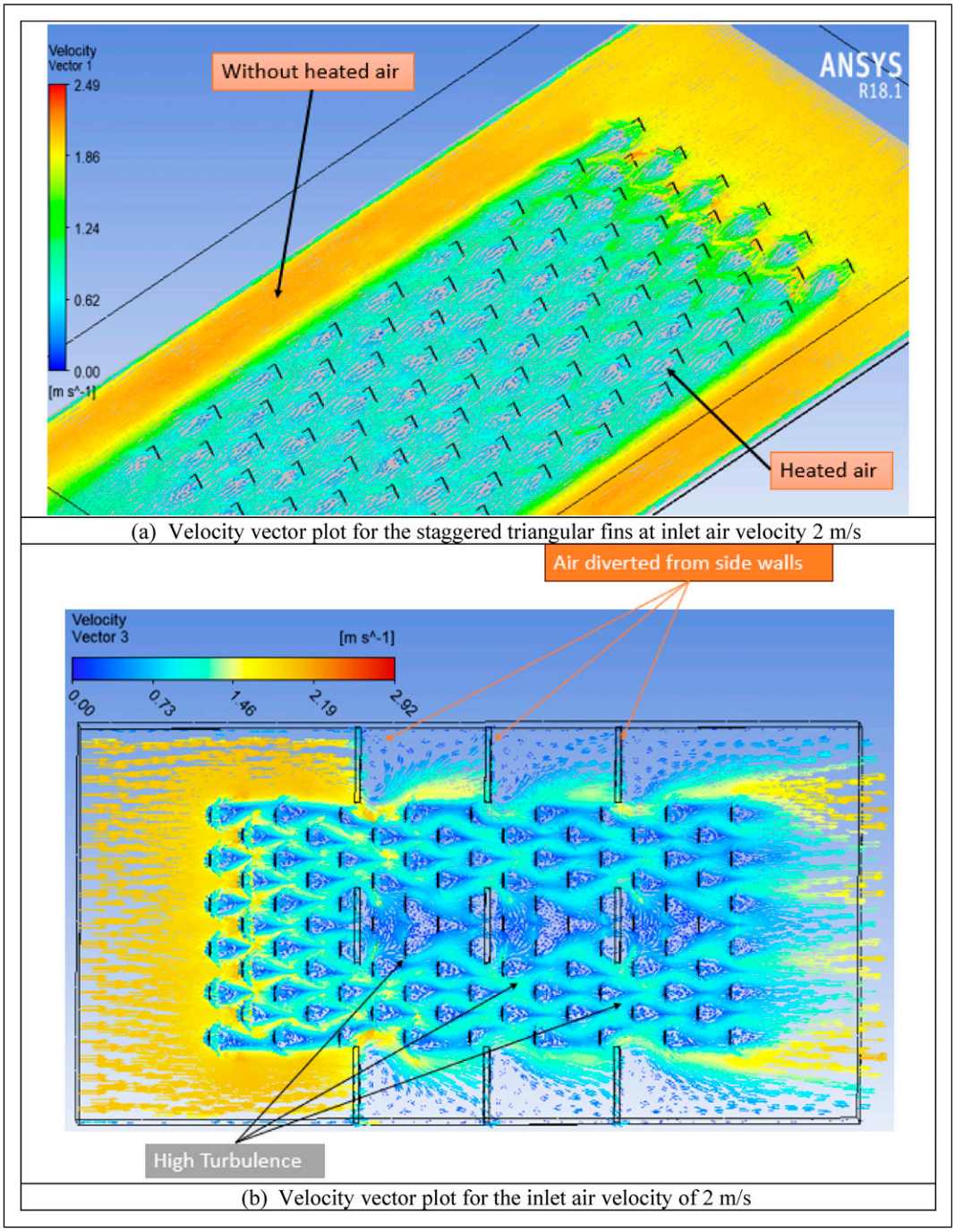

Figure 9. Velocity vector plots for the two models of the SAH.

increase in mass flow rate, which increased the heat transfer and Nusselt Number. At higher Reynolds Number, the roughened surface enhanced the skin friction drag and form drag. An increase in the overall drag increased the overall friction factor of the roughened surface, which reduced the TPF values at higher Reynolds numbers.

Graphical representation of the friction factor, Nusselt number, and TPF of TFSAH

Figure 14 represents the graphical representation of the 'f', 'Nu', and Thermal Performance Measurement with the two most important input variables, namely Re and fins pitch to height ratio. Figure 14(a) displays that if the Re increases, then the friction factor (FF) reduces. Secondly, the FF also reduces with the rise in the fins' pitch to the height ratio, since a rising pitch of the fins reduces the pressure drop; consequently, the friction factor reduces.

Figure 14(b) illustrates the Nu variation with the Re and the fins' pitch to height ratio. It is indicated from the figure that as the Re increases, the Nu increases since the turbulence is also enhanced with the Re. The Nu reduces as the fin pitch-to-height ratio increases since increasing the pitch reduces the turbulence over the surface of the SAH.

Figure 14(c) depicts that if the Re increases, the TPF values also increase due to an increase in the HT to the air. The TPF values are reduced with the increase in the pitch-

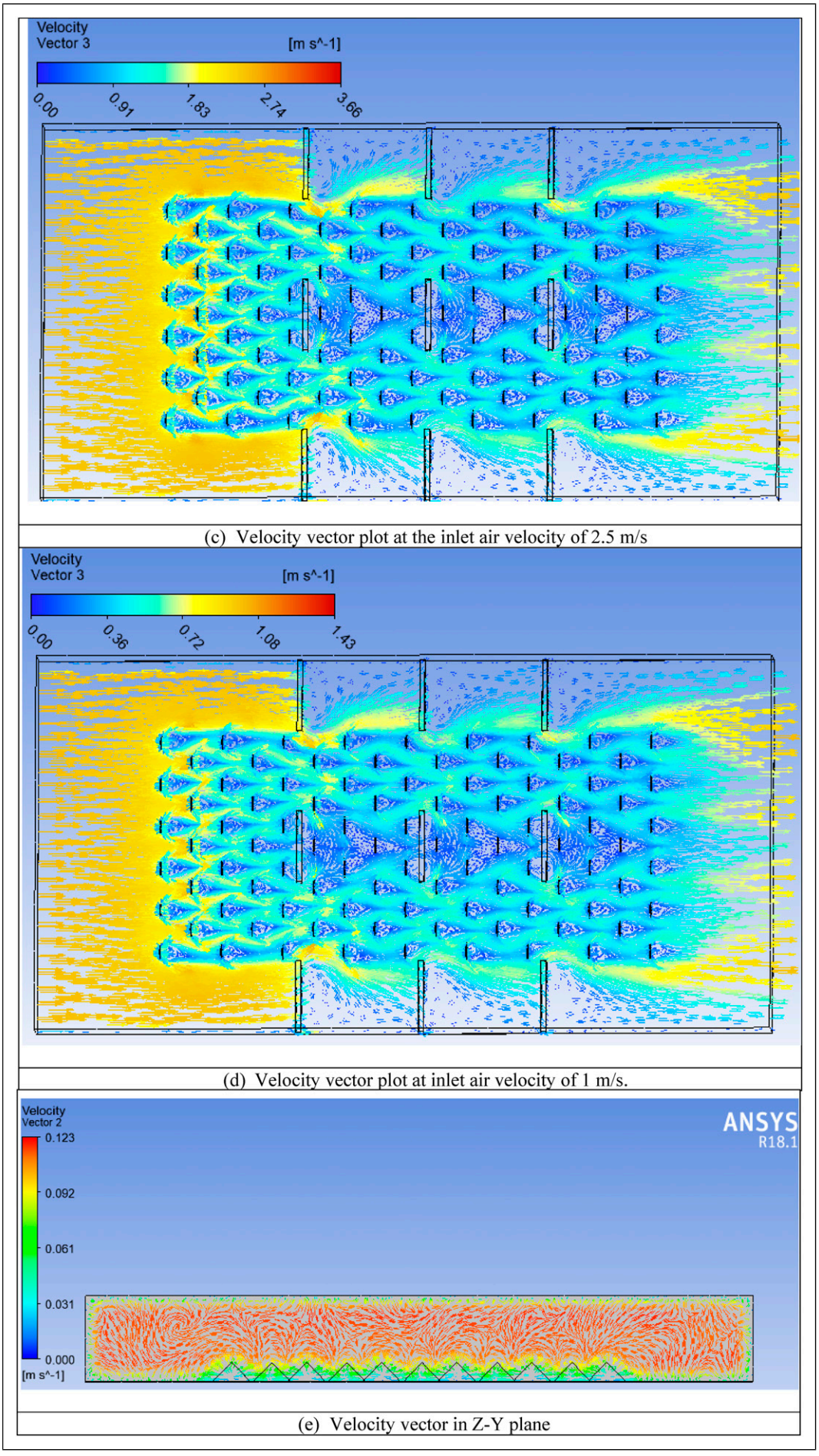

Figure 9. Continued.

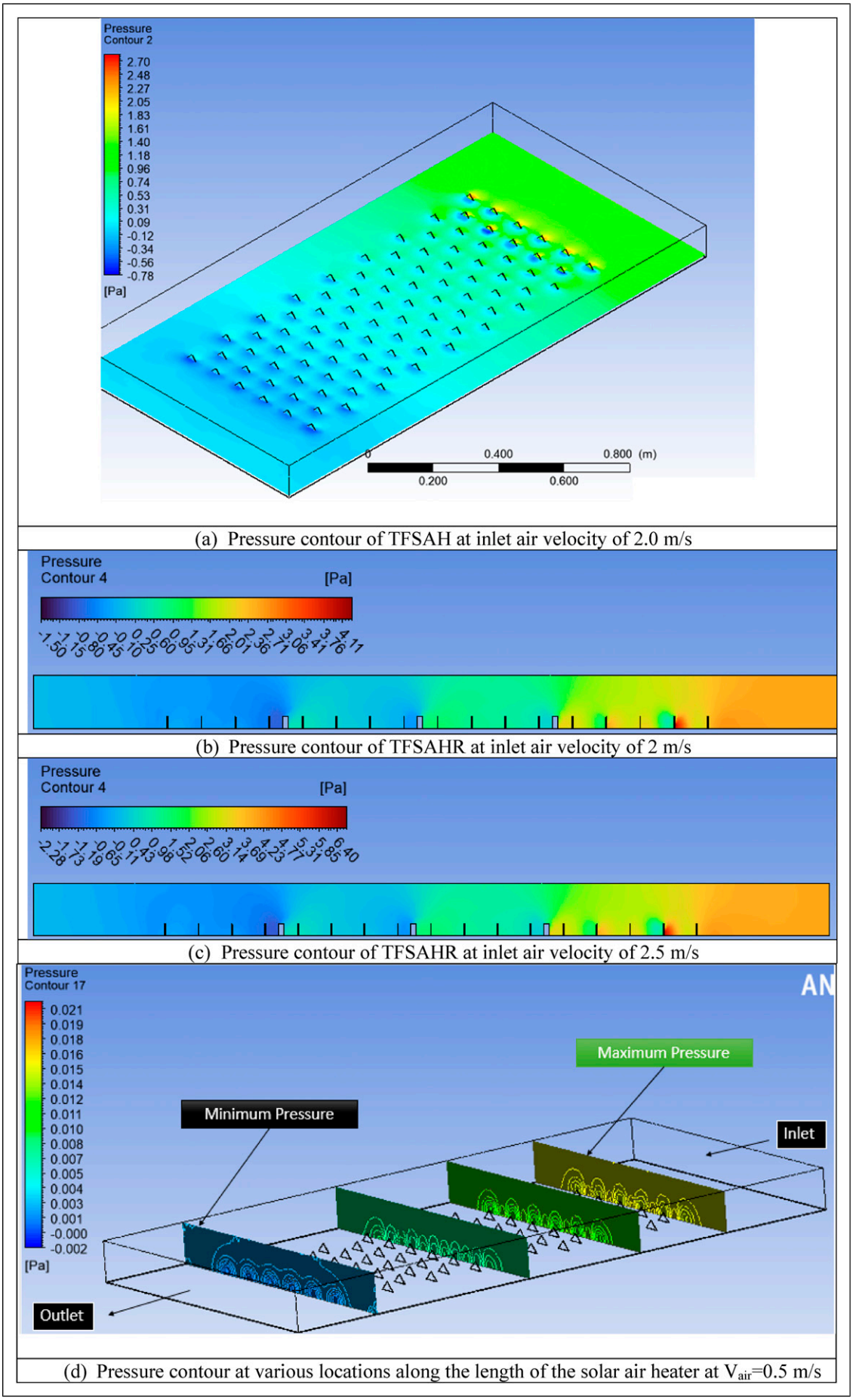

Figure 10. Pressure contour of both models.

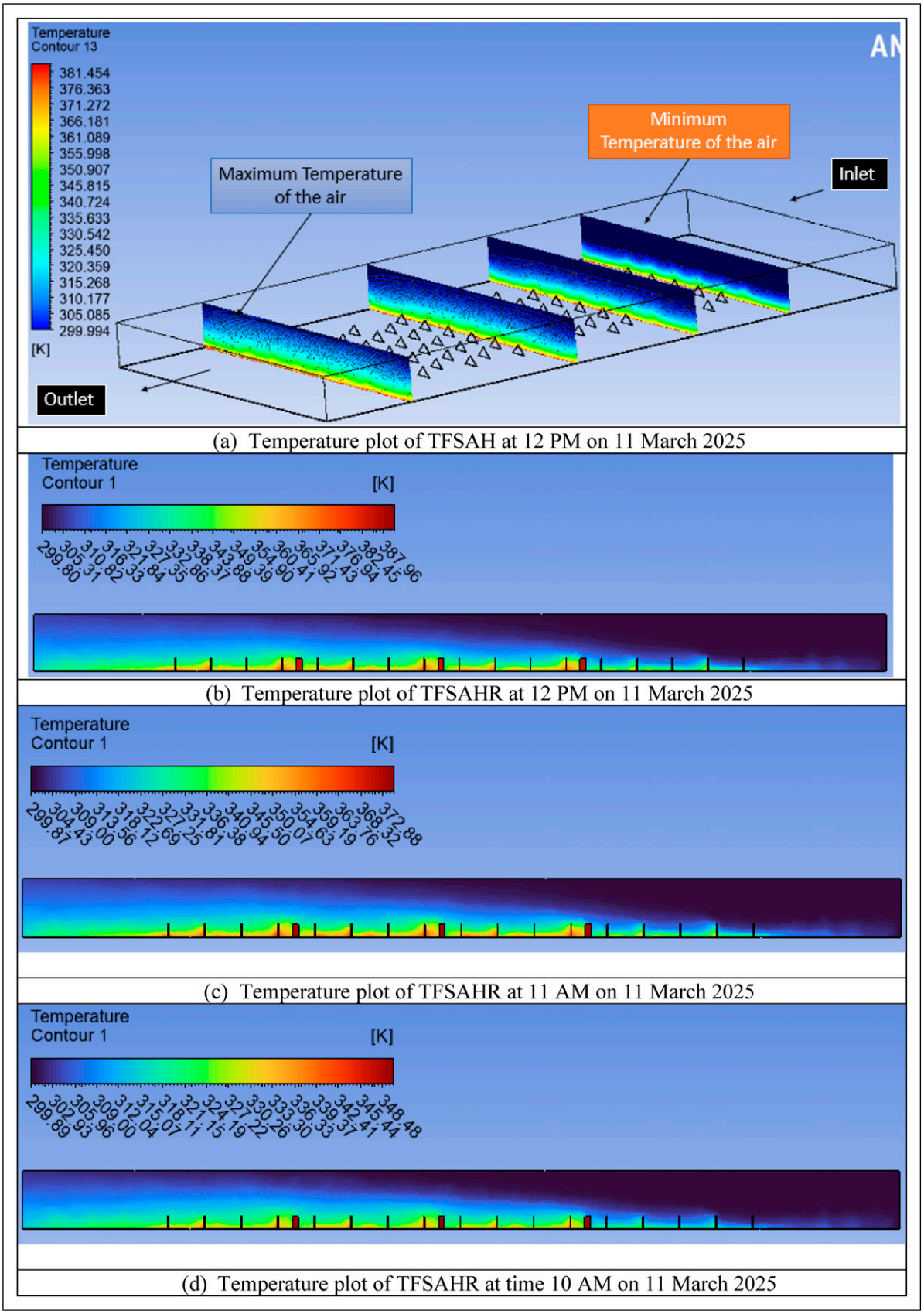

Figure 11. Temperature plot of TAFSAH and TFSAHR.

to-height ratio for all values of the Reynolds Number, since the turbulence is reduced due to the increase in the pitch. The highest value of the TPF was found to be 2.29 at the p/h value equal to 1, which is quite higher than the TPF of 1.41 of Rahmat et al. (2025)[64] in semi-stadium fins since in the semi-stadium fins the pressure drop is high as compared to TFSAH. The semi stadium fins have a higher-pressure drop than the triangular fins.

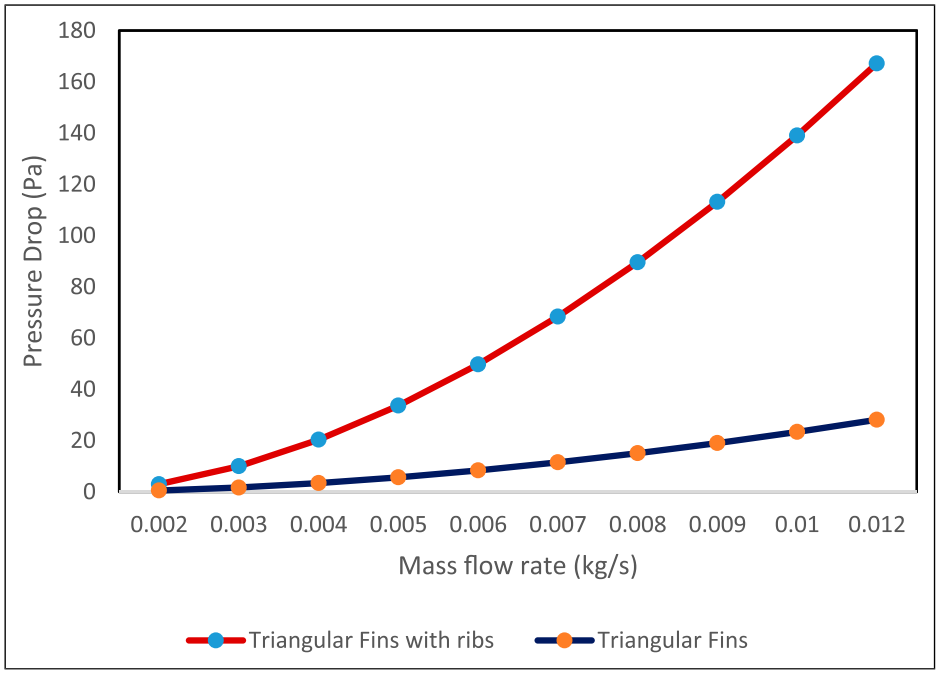

Figure 12. Pressure drop of solar heater.

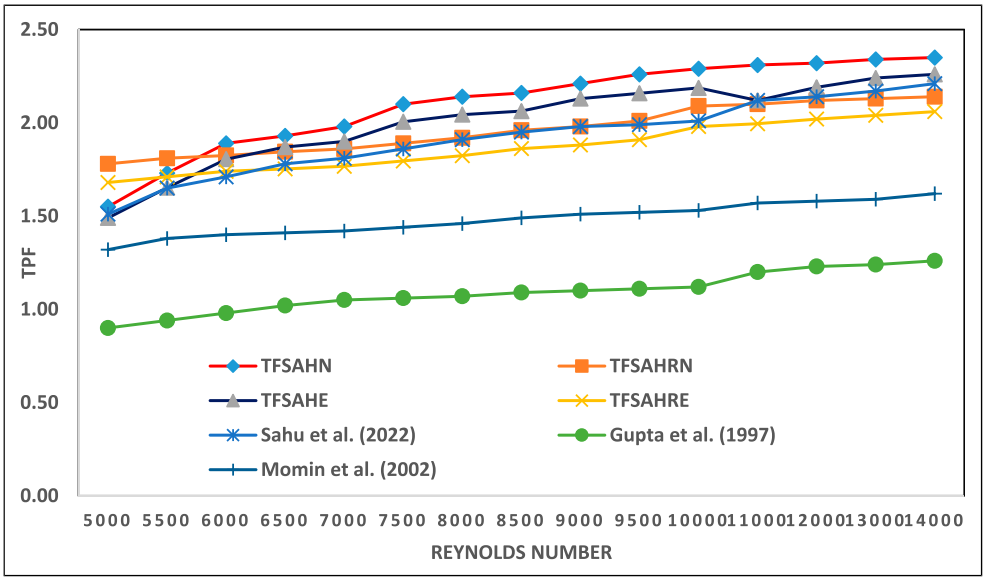

Figure 13. TPF variation with the Reynolds Number.

Heat transfer coefficient

Figure 15 represents the HTC of the absorber plate to air, glass to air, and glass to atmosphere variation with the time of day. The figure indicates the maximum HTC represented by the AP to the air and the minimum of the glass to the atmosphere. Initially, due to lower solar flux, the HTC is low, but it will increase as the heating time of the absorber plate temperature rises. The HTC mainly depends on the turbulence in the air; the maximum turbulence occurs over the surface of the AP, then between the glass and air, and the minimum turbulence is between the surface of toughened glass and the atmospheric air. The higher turbulence over the surface of the AP increases the convection and mixing of air. The triangular fins enhance the HT due to increased surface area and turbulence, consequently, higher HTC.

Validation of the thermal efficiency of the TFSAH

Figure 16 illustrates the thermal efficiency (TE) of the SAH over the day. The TE of the SAH is defined as "the ratio of the useful heat gain to the inlet solar energy supplied to the SAH". From morning to afternoon, solar flux increases, and as the solar flux increases, the useful heat gain also rises, thereby augmenting the thermal efficiency. The maximum TE was numerically and experimentally obtained to be 77.18% and 71.46%. The higher TE of SAH indicates a higher useful heat gain, which increases the temperature of the SAH at the outlet end. The thermal efficiency also depends on the mass flow rate of the air; increasing the mass flow rate of the air, the thermal efficiency also increases, the main reason behind is that augmenting the mass flow rate of air, the useful heat gain is enhanced.

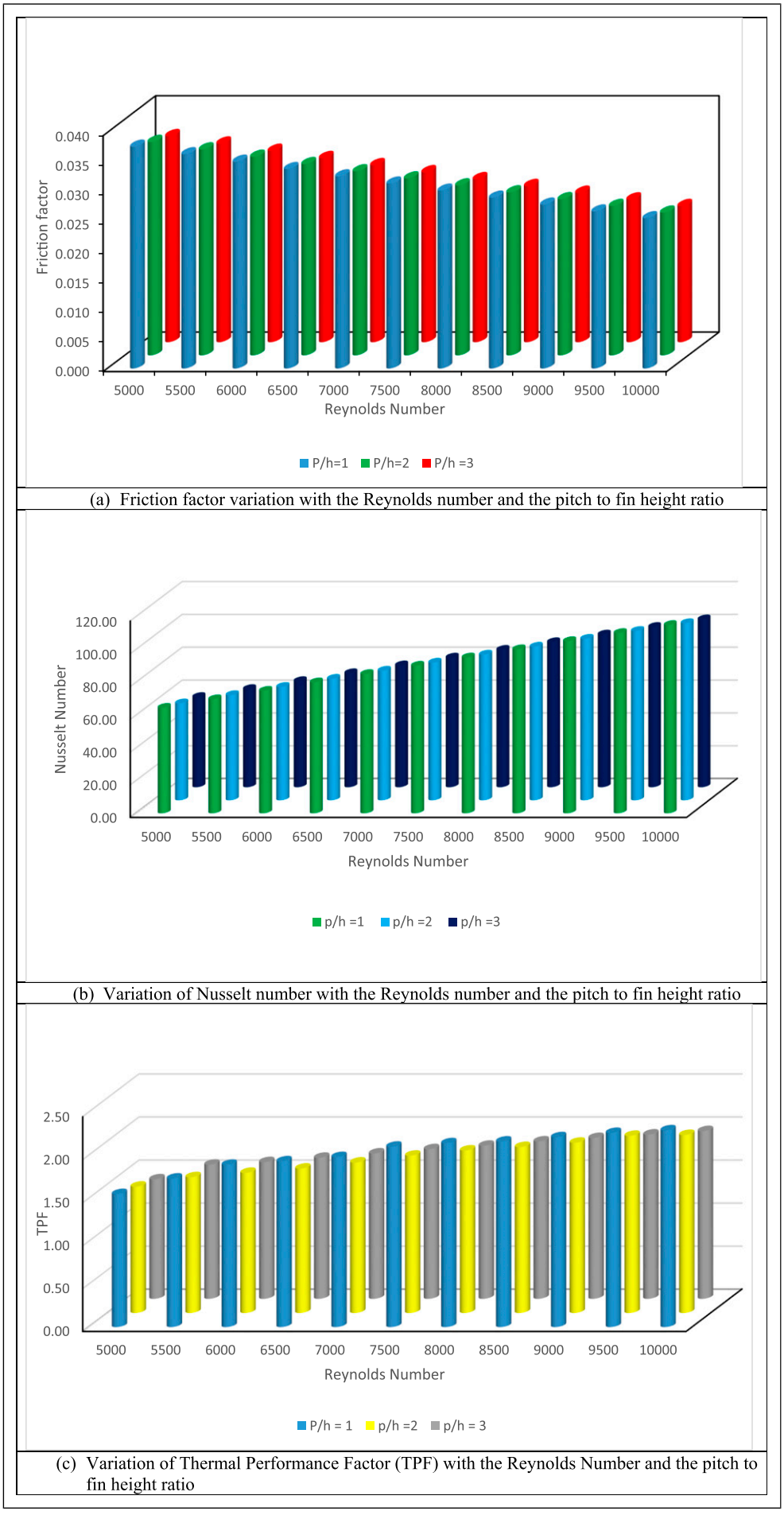

(a) Friction factor variation with the Reynolds number and the pitch to fin height ratio

(b) Variation of Nusselt number with the Reynolds number and the pitch to fin height ratio

(c) Variation of Thermal Performance Factor (TPF) with the Reynolds Number and the pitch to fin height ratio

Figure 14. Performance measurement of the solar air heater.

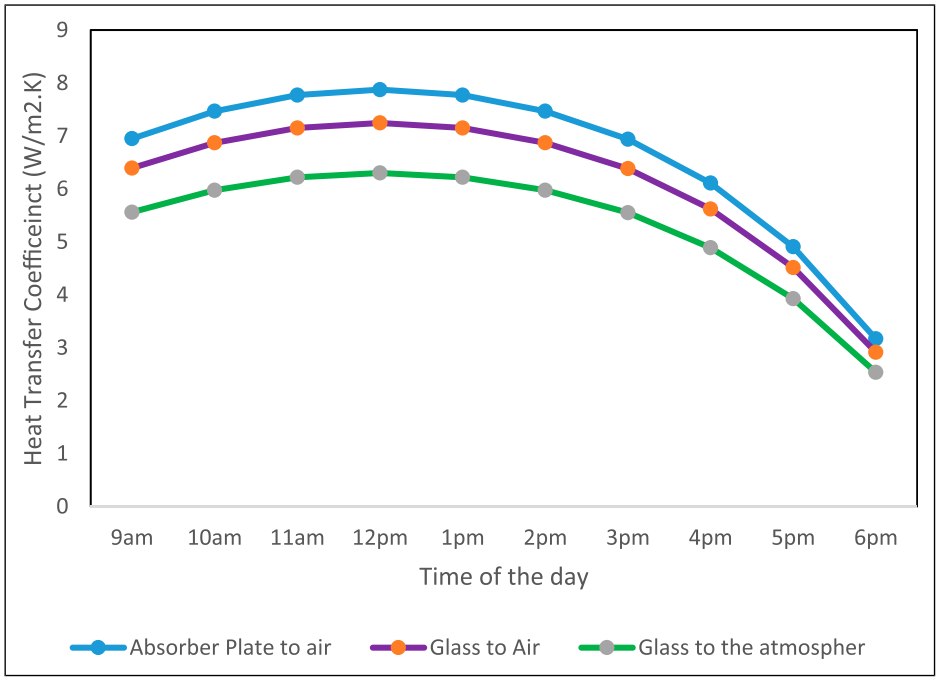

Figure 15. Heat transfer coefficient for the glass and absorber plate with the air and atmosphere.

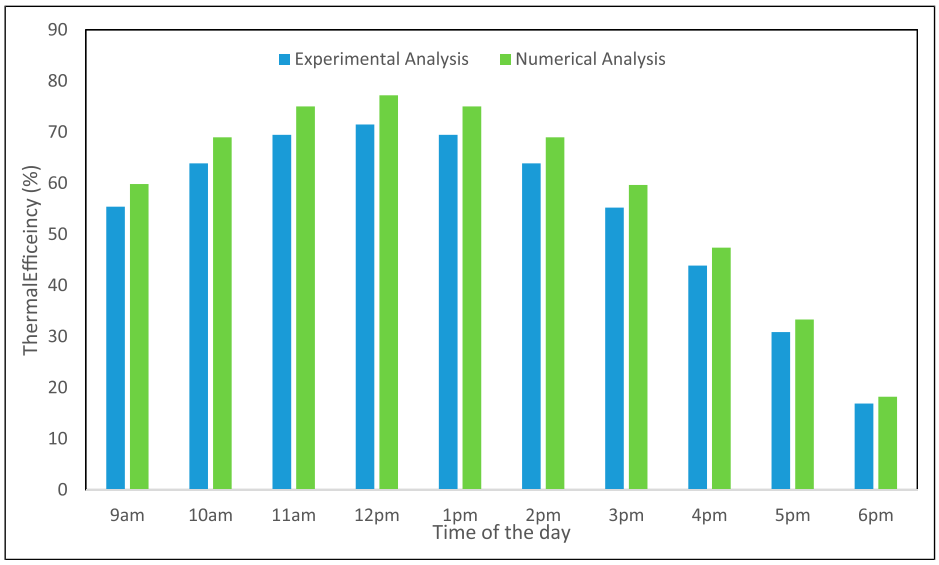

Figure 16. Thermal efficiency variation in a day.

Validation of the outlet air temperature

Figure 17 represents the outlet temperature of air from morning to evening. The highest temperature of air at the outlet was obtained to be 77.90°C and 72.25°C numerically and experimentally. The outlet air temperature will increase as the solar flux rises from morning to afternoon, then start to reduce until evening due to the reduction in solar flux. The outlet air temperature also depends on the mass flow rate of the air as the mass flow rate increases, the outlet air temperature decreases. So, outlet air temperature can be controlled by solar flux and mass flow rate.

Exergy efficiency validation

Figure 18 denotes the variation of the exergy efficiency over a day. Exergy efficiency (EE) depends on the solar flux, outlet air temperature, and absorber plate temperature. As the outlet temperature of air increases then the EE enhances. The increase in solar flux increases the quality of the air, which raises the EE. The TFSAH exergy efficiency is higher than the TFSAHR since the higher pressure drop occurs inside the TFSAHR. The maximum EE of the TFSAH and TFSAHR was obtained at noon, namely 3.94% and 3.4%.

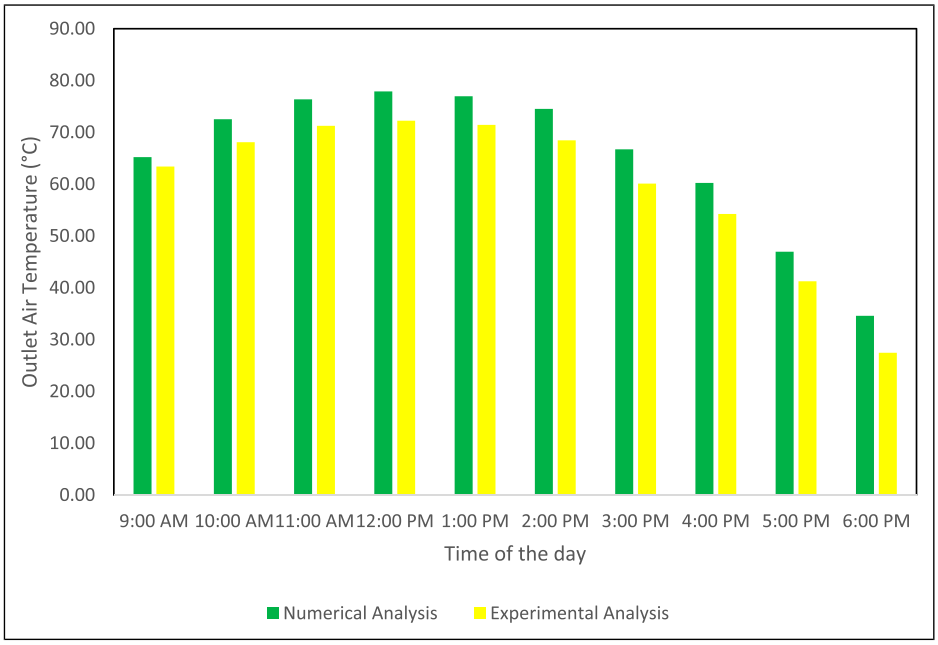

Figure 17. Outlet air temperature validation.

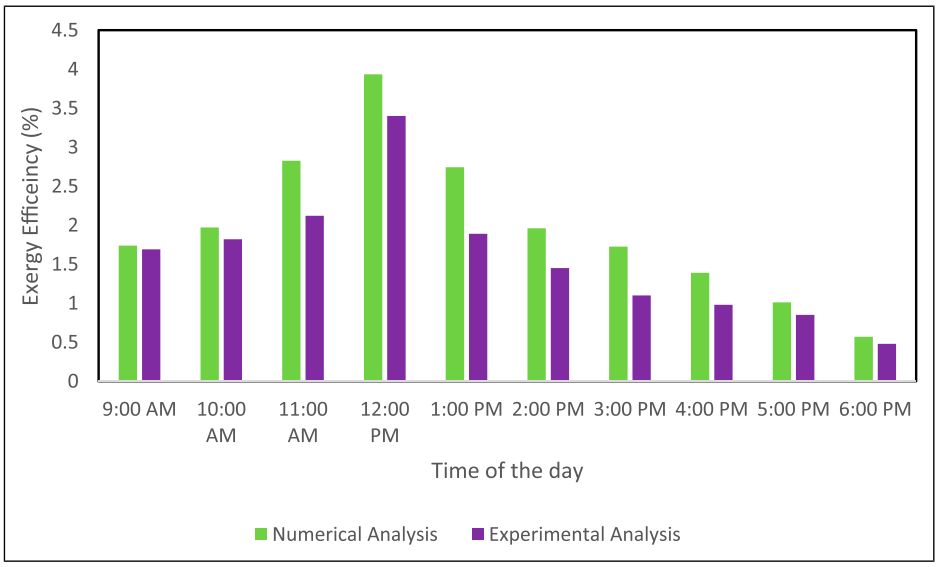

Figure 18. Exergy efficiency of the Solar Air Heater.

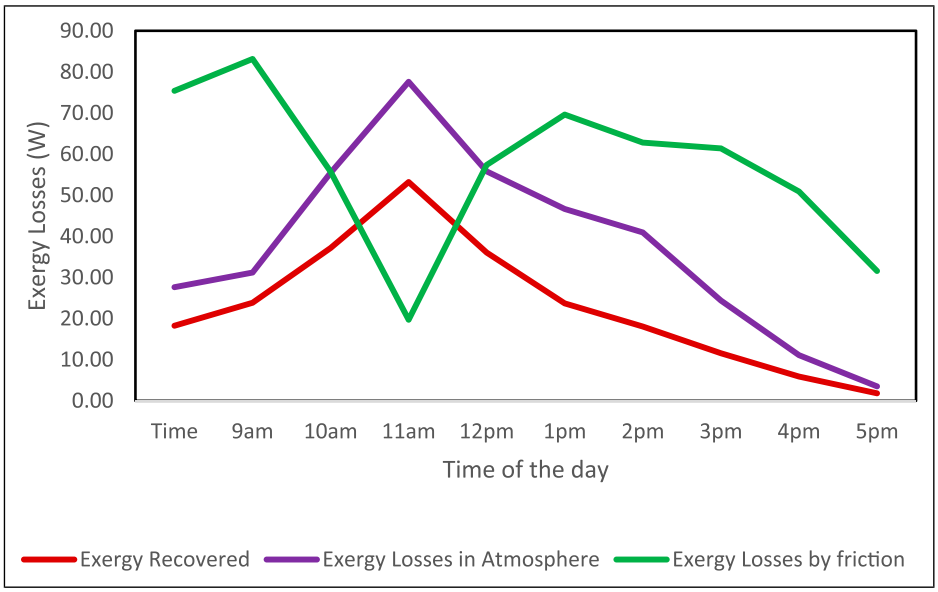

Figure 19. Various exergy losses in the SAH.

Exergy losses

Figure 19 shows the different exergy losses, namely, exergy recovered, exergy losses in the atmosphere, and the exergy losses by friction. It is indicated from the figure that the exergy recovered and exergy losses in the atmosphere are maximum at noon due to maximum solar flux, the air gains the maximum energy from the solar air heater, and it starts to reduce as the solar flux reduces. The exergy losses in the atmosphere are maximum when the absorber plate temperature is maximum, which again depends on the maximum solar flux. The exergy destruction by the friction decreases as the solar flux rises and reaches a minimum at noon, which happens due to the reduction of the friction factor as the temperature of the air increases, which makes the air lighter, leading to lower blower power.

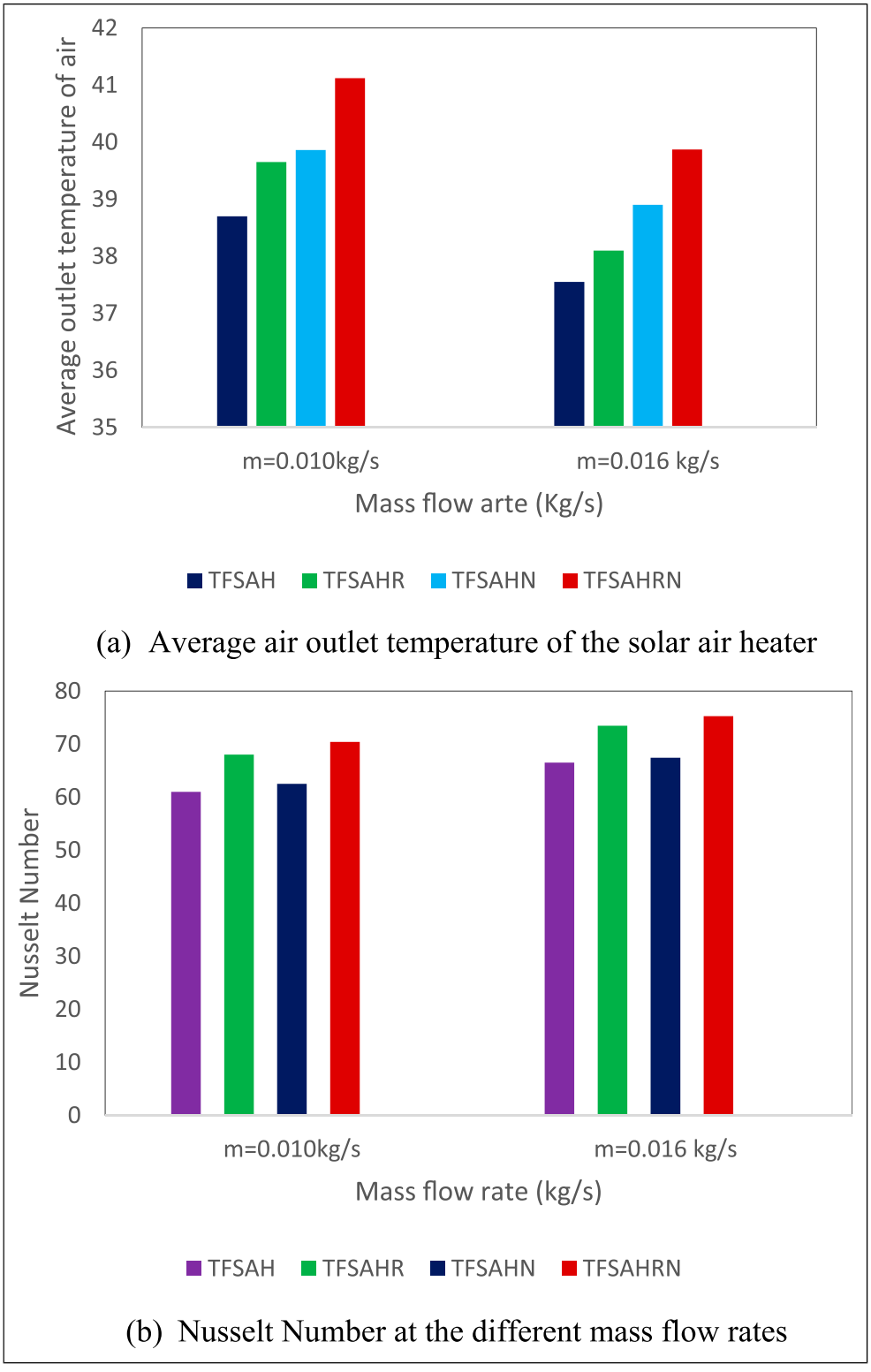

Figure 20. Validation of experimental and numerical results of average outlet temperature and Nusselt Number of SAH.

Validation of the air outlet temperature and Nusselt Number

Figure 20(a) shows the average outlet air temperature with two selected mass flow rates, 0.01 kg/s and 0.016 kg/s. The numerical studies show that in the TFSAH, the average outlet temperature of the SAH for mass flow rates of 0.01 kg/s and 0.016 kg/s is 39.86°C and 38.9°C. With the TFSAHR, the average outlet temperature with mass flow rate 0.01 kg/s and 0.016 kg/s is 41.12°C and 39.87°C. For validation of simulation results, the experiments have been performed for the mass flow rates of 0.01 kg/s and 0.016 kg/s, and determined the average outlet temperature of the SAH. Experimental results of both designs of the SAH depict that TFSAH has a lower outlet temperature of the air as compared to TFSAHR. It has been observed from the figure that the outlet air temperature for TFSAH and TFSAHR is 38.7°C and 39.65°C at the mass flow rate of 0.010 kg/s. But increasing the mass flow rate from 0.010 kg/s to 0.016 kg/s, the temperature of TFSAH and TFSAHR reduced to 37.55°C and 38.1°C. The maximum deviation of the experimental results from the simulation studies is 3%.

Figure 20(b) depicts the Nusselt Number variation with the mass flow rate of the air. Initially, the simulation study has been performed for the mass flow rate of 0.01 kg/s and 0.016 kg/s for the TFSAH and TFSAHR. It has been observed from figure that the value of the Nusselt Number for the TFSAH and TFSAHR is 62.5 and 70.4 for the mass flow rate 0.01 kg/s. These values of the Nusselt Number further increase to 67.43 and 75.25 at the mass flow rate of 0.016 kg/s. Moreover, the simulation studies are validated with the experimental results with an accuracy of the 8%.

Comparison of the thermal efficiency of the current study with previous published work

Figure 21 depicts the comparison of the current study (Triangular staggered fins) with the Brahma et al. (2024) (Phase Change Material),[65] Singh et al. (2025) (Thermoelectric generator combined with PCM),[66] Rahmat et al. (2025) (Semi-stadium shape fins),[64] Almeshaal et al. (2024) (Ring roughened finned),[67] Abdulmejeed et al. (2024) (Tripple pass V corrugated),[68] Surendhar et al. (2021) (arc rib fins)[69] and Albdoor et al. (2024) (Triangular fins).[70] It is indicated from the figure that the current study has a good thermal efficiency of 77.18% higher than the other studies due to the production of high turbulence over the surface of the absorber plate. However, the comparable thermal efficiency obtained by Brahma et al. (2024) (PCM material) and Rahmat et al. (2025) (Semi-stadium fins) of 74.25% and 75%, respectively. The thermal efficiency of the Abdulmejeed et al. (2024) (Triple pass V corrugated)[68] have quite low thermal efficiency due to a huge pressure drop in triple pass and dense V corrugated projection.

Validation of the present study with suresh et al. (2022)[71]

Validation of the Nusselt Number, TPF and exergy efficiency. Figure 22 depicts the validation of the Nusselt Number, TPF, and exergy efficiency of the trapezoidal rib's absorber plate SAH research published by Suresh et al. (2022)[71] with the present study. Figure 22(a) shows that as the Reynolds Number increases, the Nusselt Number increases in both designs. The maximum value of the Nusselt Number in Suresh et al. (2022) and the current

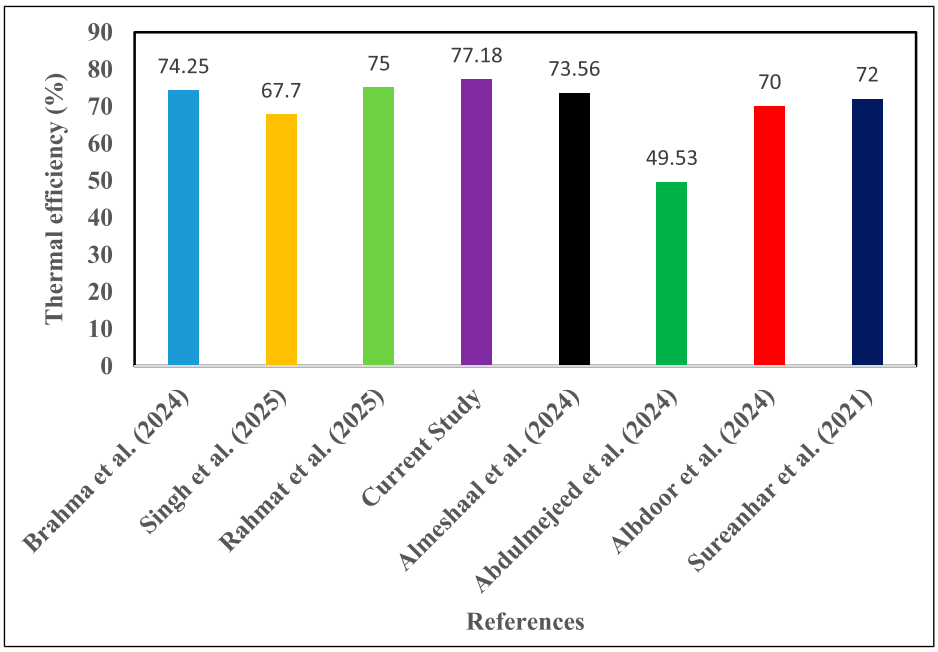

Figure 21. Thermal efficiency validation of the current study with previous work.

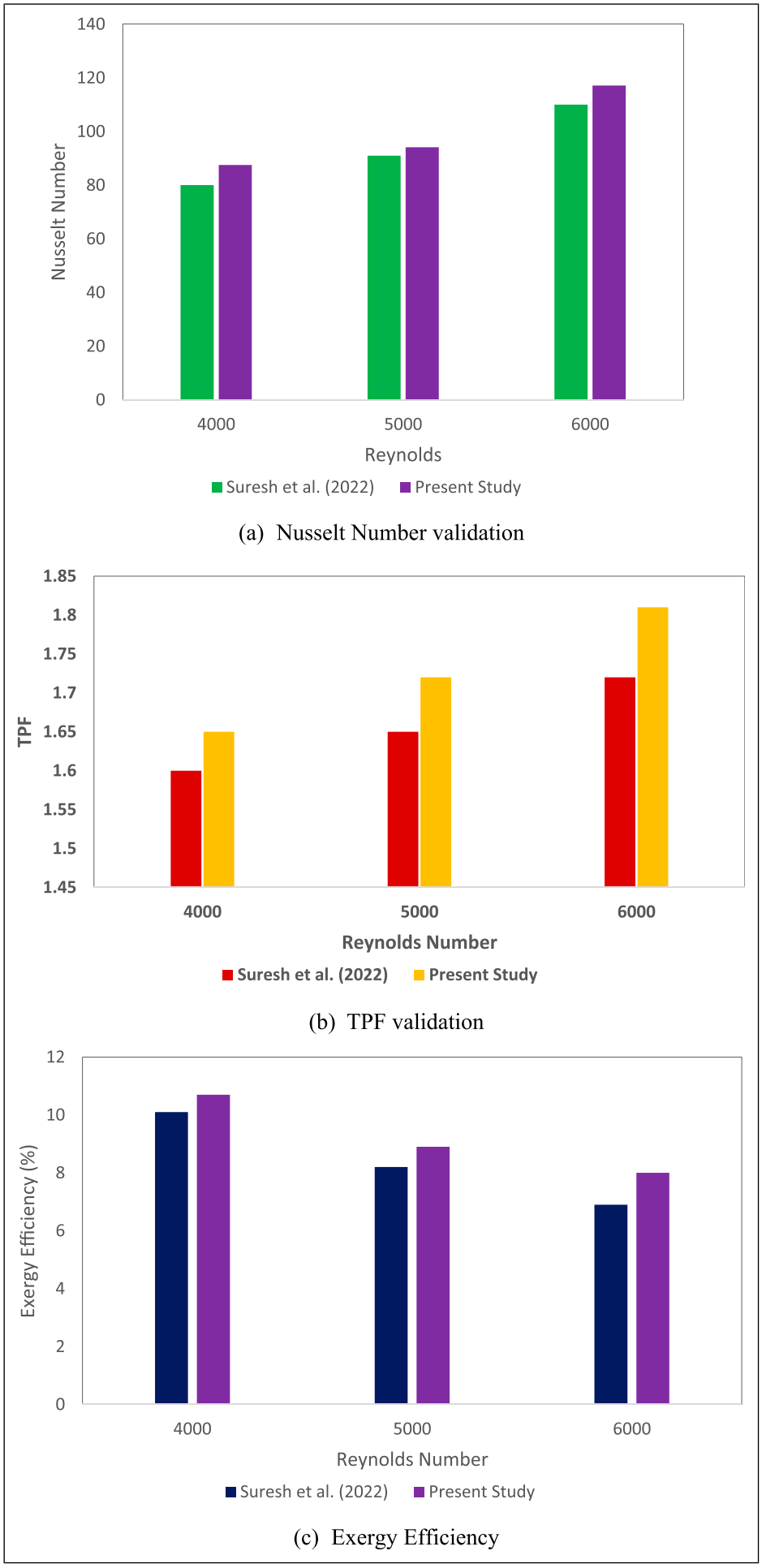

Figure 22. Validation of Nusselt number, TPF, and exergy efficiency at 1000 W/m^2.

study is 110 and 117.12 at Reynolds Number 6000. Figure 22(b) demonstrated that TPF values also increase as the Reynolds Number increases, with the maximum TPF obtained as 1.81 and 1.72 in the present study and Suresh et al. (2022) at 6000 Reynolds Number. Figure 22(c) illustrates the exergy efficiency validation, it is observed from the figure that as the Reynolds Number increases, the exergy efficiency reduces due to enhanced blower electric power. The maximum efficiency obtained was 10.7 and 10.1 at the Reynolds Number 400 and solar flux 1000 W/m^2.

The error analysis is calculated in the form of Root Mean Square Error (RMSE) and Mean Absolute Error (MAE). Table 7 represents the error analysis of Nusselt Number, TPF and Exergy Analysis in term of RMSE and MAE.

Table 7. Error analysis.

Parameter	RMSE	MAE
Nusselt number	6.23	5.9
TPF	0.071	0.07
Exergy efficiency	1.43	0.8

Validation of average outlet temperature and Nusselt Number of current study with Khanlari et al. (2023)[35]. Figure 23 represents the average outlet temperature and Nusselt Number validation of the present study with that Khanlari et al. (2023)[35] at the mass flow rates of 0.01 kg/s and 0.016 kg/s. The maximum outlet temperature of TFSAHR and TFSAH is 39.67°C and 38.7°C as compared to 38.5°C

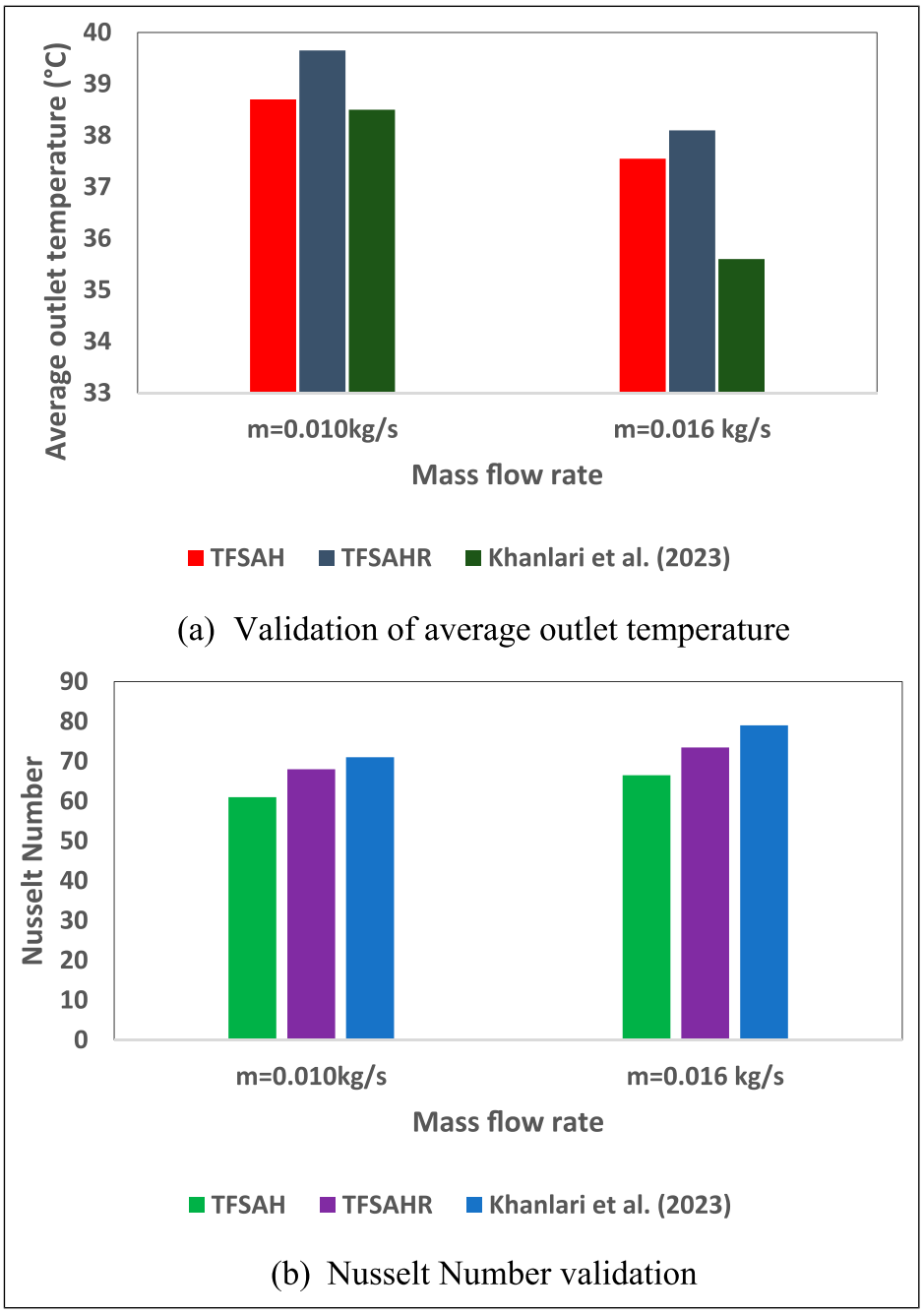

Figure 23. Validation of the TFSAH, TFSAHR with Khanlari et al. (2023).

in Khanlari et al. (2023) at a mass flow rate of 0.01 kg/s as presented in Figure 23(a). Increasing the mass flow rate of SAH from 0.01 kg/s to 0.016 kg/s, the average outlet temperature reduced. The main region behind is that, the surface area of Khanlari et al (2023) have lower surface area as compared to the present study of TFSAH and TFSAHR. The Khanlari et al. (2023) have the surface area of 0.24 m^2 as compared study 1.26 m^2 but effective utilisation of the solar energy due to use of the aluminium cans.

On another side compared to Nusselt Number, the Khanlari et al. (2023) have larger value with the TFSAH and TFSAHR since the higher heat transfer coefficient as shown in Figure 23(b). Khanlari et al. (2023) have higher heat transfer coefficient due to smaller surface area as compared to the TFSAH and TFSAHR.

Conclusion

This section concludes the key features of the Experimental and Numerical investigation focused on the TFSAH and TFSAHR. The conclusion centred around the numerical findings to find the best one from the TFSAH and the TFSAHR. The effect of the ribs fixed at the inner periphery of the SAH so that unaffected air will diverge on the triangular fins and enhance the turbulence and heat transfer. The following points has to be concluded from this study.

(1) The simulation results of the TFSAH shows that a lot of amounts of unheated air flows through the side wall of the SAH. So, for fixing the ribs on the sides of the SAH, divert the air to forced flow through the triangular section and heat it, which increases the turbulence and the heat transfer to the air.
(2) The increasing ribs on the side walls of the SA also increase the pressure drop which reduce the thermal performance factor. Based on the TPF comparison, the triangular fins give better performance than the TFSAH after crossing the Reynolds Number from 6000.
(3) The pressure drops in TFSAH and TFSAHR is 2.79 Pa and 3.19 Pa at 2.0 m/s inlet air velocity.
(4) The maximum temperature of the TFSAH and TFSAHR on 11 March 2025 at 12 p.m. is 381.49 K and 393 K.
(5) The rise in Reynolds number decreases the friction factor, but the Nusselt number and TPF increase for a triangular fin SAH. The maximum values of the Nu and TPF obtained are 114.95 and 1.89 for the Reynolds Number 10,000 and P/h ratio of 1. The minimum friction factor reached 0.023 at a Reynolds number of 10,000 and a P/h ratio of 3.
(6) The simulation results are validated with the experimental results on the date 11/03/2025. The maximum temperature of air at the outlet, Thermal Efficiency, and exergy obtained through the experimental observation are 72.25°C, 77.18%, and 3.4% at noon at an MFR of 0.08 kg/s. The simulation results are validated with the experimental results within an accuracy of 5%.

Limitations of the study and source of uncertainty

The SAH is very useful where low and moderate-temperature air is required. It can be used to warm the building, crop drying, and processing of food. Despite so many benefits, it has some limitations. Due to the lower thermal properties of air, the heat transfer to air is low. For increasing the heat transfer, rate fins and ribs are added, which increase the design complication and require higher blower power. Furthermore, increasing the blower power reduced the net thermal efficiency, exergy efficiency, and TPF values. So, in the present study, it has been concluded that if the TFSAHR has worked well upto 6000 Reynolds Number. If further Reynolds number increases, then the ribs should be removed. Additionally, only triangular fins SAH performance is good upto 1000 Reynolds Number.

The main source of uncertainty is due to experimental observations, which are mainly used to calculate the performance of the SAH, namely, thermal efficiency, heat transfer, Nusselt Number, and TPF calculations. Measurement of inlet air and outlet temperature, mass flow rate, and solar radiation through the instruments always has some uncertainty that is considered as the main source of uncertainty. The secondary source of the uncertainty is the non-uniform inlet air conditions and heat losses from the side walls of the SAH.

Declaration of conflicting interests

The authors declared no potential conflicts of interest with respect to the research, authorship, and/or publication of this article.

Funding

The authors received no financial support for the research, authorship, and/or publication of this article.

ORCID iD

Vineet Singh https://orcid.org/0000-0003-3328-2588

References

1. Hussin F, Issabayeva G and Aroua MK. Solar photovoltaic applications: opportunities and challenges. *Rev Chem Eng* 2018; 34(4): 503–528. https://doi.org/10.1515/REVCE-2016-0058
2. Ghasemzadeh F, Ghasemzadeh F, Shayan ME, et al. Nanotechnology in the service of solar energy systems. *J Environ Nanotechnol*. 2020; 10: 1–10. https://doi.org/10.5772/INTECHOPEN.93014
3. Tyagi VV, Panwar NL, Rahim NA, et al. Review on solar air heating system with and without thermal energy storage system. *Renew Sustain Energy Rev* 2012; 16(4): 2289–2303. https://doi.org/10.1016/J.RSER.2011.12.005
4. Maradin D. Advantages and disadvantages of renewable energy sources utilization. *Int J Energy Econ Pol* 2021; 11(3): 176–183. https://doi.org/10.32479/ijeep.11027
5. Uddin I. Optimization of a hybrid system connected with utility grid using homer software. *Int J Eng Works* 2019; 06(12): 525–528. https://doi.org/10.34259/IJEW.19.612525528
6. Elbrashy A, Aboutaleb F, El-Fakharany M, et al. Experimental study of solar air heater performance with evacuated

tubes connected in series and involving nano-copper oxide/paraffin wax as thermal storage enhancer. *Environ Sci Pollut Control Ser* 2023; 30(2): 4603–4616. https://doi.org/10.1007/s11356-022-22462-6
7. Mahboub C, Moummi N, Brima A, et al. Experimental study of new solar air heater design. *Int J Green Energy* 2016; 13(5): 521–529. https://doi.org/10.1080/15435075.2014.968922
8. Kalogirou SA. Solar thermal collectors and applications. *Prog Energy Combust Sci* 2004; 30(3): 231–295. https://doi.org/10.1016/j.pecs.2004.02.001
9. Albdoor AK, Obaid ZAH, Kamel MS, et al. Energy, exergy, economic and environmental analysis of a solar air heater integrated with double triangular fins: experimental investigation. *Int J Thermofluids* 2024; 24: 100979. https://doi.org/10.1016/j.ijft.2024.100979
10. Bezbaruah PJ, Das A, Das RS, et al. Numerical investigation on triangular fin-based solar air heater. In: *Advances in Energy Research*, (Vol. 2). Springer, 2020. https://doi.org/10.1007/978-981-15-2662-6_31
11. Michael Joseph Stalin P, Rao PN, Palaniappan M, et al. Effective thermal performance assessment for prismatic triangular solar air heater integrated with fins and turbulators. *Numeri Heat Transf A Appl* 2024; 86: 8129–8145. https://doi.org/10.1080/10407782.2024.2357592
12. Kumar R and Verma SK. Numerical investigation of performance analysis of triangular solar air heater using Computational Fluid Dynamics (CFD). *IOP Conf Ser Mater Sci Eng* 2021; 1116(1): 012047. https://doi.org/10.1088/1757-899x/1116/1/012047
13. Guardo A, Coussirat M, Valero C, et al. CFD assessment of the performance of lateral ventilation in double glazed façades in mediterranean climates. *Energy Build* 2011; 43(9): 2539–2547. https://doi.org/10.1016/j.enbuild.2011.06.008
14. Akhbari M, Rahimi A and Hatamipour MS. Modeling and experimental study of a triangular channel solar air heater. *Appl Therm Eng* 2020; 170: 114902. https://doi.org/10.1016/j.applthermaleng.2020.114902
15. Chang W, Wang Y, Li M, et al. The theoretical and experimental research on thermal performance of solar air collector with finned absorber. *Energy Proc* 2015; 70: 13–22. https://doi.org/10.1016/j.egypro.2015.02.092
16. Singh V, Yadav VS, Trivedi V, et al. Application of response surface methodology for analysing and optimizing the finned solar air heater. *J Therm Sci* 2024; 33(3): 985–1009. https://doi.org/10.1007/s11630-024-1934-z
17. Manjunath MS, Karanth KV and Sharma NY. Numerical analysis of the influence of spherical turbulence generators on heat transfer enhancement of flat plate solar air heater. *Energy* 2017; 121: 616–630. https://doi.org/10.1016/j.energy.2017.01.032
18. Cj T, Matheswaran MM, Gnanasekaran N, et al. Analytical investigation on thermo hydraulic performance augmentation of triangular duct solar air heater integrated with wavy fins. *Int J Green Energy* 2023; 20(5): 544–554. https://doi.org/10.1080/15435075.2022.2111215
19. Kumar S and Saini RP. CFD based performance analysis of a solar air heater duct provided with artificial roughness. *Renew Energy* 2009; 34(5): 1285–1291. https://doi.org/10.1016/j.renene.2008.09.015
20. Boulemtafes-Boukadoum A, Abid C and Benzaoui A. 3D numerical study of the effect of aspect ratio on mixed convection air flow in upward solar air heater. *Int J Heat Fluid Flow* 2020; 84: 108570. https://doi.org/10.1016/j.ijheatfluidflow.2020.108570
21. Nidhul K, Kumar S, Yadav AK, et al. Enhanced thermo-hydraulic performance in a V-ribbed triangular duct solar air heater: CFD and exergy analysis. *Energy* 2020; 200: 117448. https://doi.org/10.1016/j.energy.2020.117448
22. Xiao H, Wang J, Liu Z, et al. Turbulent heat transfer optimization for solar air heater with variation method based on exergy destruction minimization principle. *Int J Heat Mass Tran* 2019; 136: 1096–1105. https://doi.org/10.1016/j.ijheatmasstransfer.2019.03.071
23. Ansari M and Bazargan M. Optimization of flat plate solar air heaters with ribbed surfaces. *Appl Therm Eng* 2018; 136: 356–363. https://doi.org/10.1016/j.applthermaleng.2018.02.099
24. Sharma M and Bhargva M. CFD based performance analysis of solar air heater provided with artificial roughness in the form of V – shaped ribs. *Mater Today Proc* 2022; 63: 595–601. https://doi.org/10.1016/j.matpr.2022.04.168
25. Singh I and Singh S. CFD analysis of solar air heater duct having square wave profiled transverse ribs as roughness elements. *Sol Energy* 2018; 162: 442–453. https://doi.org/10.1016/j.solener.2018.01.019
26. Kumar S, Kumar U, Piyush, et al. CFD analysis of the influence of distinct thermal enhancement techniques on the efficiency of Double Pass Solar Air Heater (DP-SAH). *Mater Today Proc* 2023. https://doi.org/10.1016/j.matpr.2023.05.454
27. Kumar N, Singh MK, Yadav VS, et al. A comparative analysis of ribs and cans type solar air heater. *Evergreen* 2023; 10(3): 1449–1459. https://doi.org/10.5109/7151694
28. Velmurugan P and Kalaivanan R. Energy and Exergy Analysis of Solar Air Heaters with Varied Geometries. *Arabian Journal for Science and Engineering*. 2015; 40: 1173–1186.
29. Khanlari A and Tuncer AD. Analysis of an infrared-assisted triple-flow prototype solar drying system with nano-embedded absorber coating: an experimental and numerical study. *Renew Energy* 2023; 216(Nov): 119125. https://doi.org/10.1016/j.renene.2023.119125
30. Sahu MK, Sharma M, Matheswaran MM, et al. On the use of longitudinal fins to enhance the performance in rectangular duct of solar air heaters - a review. *J Sol Energy Eng* 2019; 141(3): 030802. https://doi.org/10.1115/1.4042827
31. Qader BS, Supeni EE, Ariffin MKA, et al. RSM approach for modeling and optimization of designing parameters for inclined fins of solar air heater. *Renew Energy* 2019; 136: 48–68. https://doi.org/10.1016/j.renene.2018.12.099
32. Yadav AS and Bhagoria JL. A CFD (computational fluid dynamics) based heat transfer and fluid flow analysis of a solar air heater provided with circular transverse wire rib roughness on the absorber plate. *Energy* 2013; 55: 1127–1142. https://doi.org/10.1016/j.energy.2013.03.066
33. Pratap Singh jeet and Singh OP. Performance enhancement of a curved solar air heater using CFD. *Solar Energy*. 2018; 174: 556–569.
34. Khanlari A, Aytaç İ, Tuncer AD, et al. Improving the performance of a PCM integrated solar air collector by adding

porous fins over the bottom side of the absorber: a transient CFD study. *J Energy Storage*. 2024; 90: 1–20. https://doi.org/10.1016/j.est.2024.111847
35. Khanlari A, Tuncer AD, Afshari F, et al. Utilization of recyclable aluminum cans as fins in a vertical solar air heating system: an experimental and numerical study. *J Build Eng* 2023; 63: 105446. https://doi.org/10.1016/j.jobe.2022.105446
36. Huddar VB, Razak A, Cuce E, et al. Thermal performance study of solar air dryers for cashew kernel: a comparative analysis and modelling using Response Surface Methodology (RSM) and artificial neural network (ANN). *Int J Photoenergy* 2022; 2022: 1–18. https://doi.org/10.1155/2022/4598921
37. Elmasry Y, Chaturvedi R, Ali A, et al. Engineering analysis with boundary elements numerical analysis and RSM modeling of the effect of using a V-cut twisted tape turbulator in the absorber tube of a photovoltaic/thermal system on the energy and exergy performances of the system. *Eng Anal Bound Elem* 2023; 155(June): 340–350. https://doi.org/10.1016/j.enganabound.2023.06.013
38. Sivakumar S, Siva K and Mohanraj M. Experimental thermodynamic analysis of a forced convection solar air heater using absorber plate with pin-fins. *J Therm Anal Calorim* 2019; 136(1): 39–47. https://doi.org/10.1007/s10973-018-07998-5
39. Din SIU, Ibrahim A, Ajeel RK, et al. Thermal performance analysis of a double-pass solar air heater with lava rock as porous and sensible heat storage material. *J Energy Storage* 2024; 95(June): 112564. https://doi.org/10.1016/j.est.2024.112564
40. Zhang Y, Li R, Zhang B, et al. Design and performance analysis of 15MWth SCO2-cooled micro reactor. *Nucl Eng Technol* 2025; 57(12): 103863. https://doi.org/10.1016/j.net.2025.103863
41. Qi H, Zhou Y, Zhang Z, et al. Heat transfer performance in energy piles in urban areas: case studies for lambeth college and shell centre UK. *Appl Sci* 2020; 10(17): 5974. https://doi.org/10.3390/app10175974
42. Singh V, Yadav VS, Trivedi V, et al. Application of response surface methodology for analysing and optimizing the finned solar air heater. *J Therm Sci* 2024; 33(3): 985–1009. https://doi.org/10.1007/s11630-024-1934-z
43. Kumar S, Das RK, Kulkarni K, et al. Designing of low cost solar air heater equipped with roughness of streamlined cross-section. *Case Stud Therm Eng* 2023; 45: 102915. https://doi.org/10.1016/j.csite.2023.102915
44. Singh H, Kishore C, Chamoli S, et al. Environmental effects enhancing heat transfer in rectangular solar air heater channels: a numerical exploration of multiple Boomerang-shaped roughness elements with variable gaps. *Energy Sources, Part A Recovery, Util Environ Eff* 2024; 46(1): 6696–6712. https://doi.org/10.1080/15567036.2024.2354506
45. Miao L, Wan R, Wu H, et al. Heat transfer and pressure drop characteristic research of sine wavy flying - wing fins. *Sci Rep* 2023; 13: 1–14. https://doi.org/10.1038/s41598-023-42872-x
46. Alsaiari AO, Alzahrani HAH, Madhukeshwara N, et al. Heat transfer augmentation in a solar air heater with conical roughness elements on the absorber. *Case Stud Therm Eng* 2022; 36(April): 102210. https://doi.org/10.1016/j.csite.2022.102210
47. Sharma A, Thakur S, Dhiman P, et al. Effect of jet-impingement and surface roughness on performance of solar air heater: experimental study and its optimization. *Expert Syst Appl* 2024; 238(PE): 122208. https://doi.org/10.1016/j.eswa.2023.122208
48. Pandey R. Effect of pitch and hole-hydraulic depth of perforated V-shaped baffles on the heat transfer and thermo-hydraulic performance of an air heater duct. *Proc Inst Mech Eng Part E J Process Mech Eng* 2023; 238: 1647–1664. https://doi.org/10.1177/09544089231157977
49. Kanargi OB, Lee PS and Yap C. A numerical and experimental investigation of heat transfer and fluid flow characteristics of a cross-connected alternating converging–diverging channel heat sink. *Int J Heat Mass Tran* 2017; 106: 449–464. https://doi.org/10.1016/j.ijheatmasstransfer.2016.08.057
50. Du J, Chen H, Li Q, et al. Turbulent flow-thermal-thermodynamic characteristics of a solar air heater with spiral fins. *Int J Heat Mass Tran* 2024; 226(March): 125434. https://doi.org/10.1016/j.ijheatmasstransfer.2024.125434
51. Borah PP, Pathak KK, Gupta A, et al. Experimental study of a solar air heater with modified absorber plate through square obstacles with threaded pin fins. *Appl Therm Eng* 2023; 228(March): 120544. https://doi.org/10.1016/j.applthermaleng.2023.120544
52. Akhbari M, Rahimi A and Hatamipour MS. Modeling and experimental study of a triangular channel solar air heater. *Appl Therm Eng* 2020; 170(December 2019): 114902. https://doi.org/10.1016/j.applthermaleng.2020.114902
53. Naphon P. On the performance and entropy generation of the double-pass solar air heater with longitudinal fins. *Renew Energy* 2005; 30: 1345–1357. https://doi.org/10.1016/j.renene.2004.10.014
54. Yusuf A, Bayhan N, Tiryaki H, et al. Multi-objective optimization of concentrated photovoltaic-thermoelectric hybrid system via Non-Dominated Sorting Genetic Algorithm (NSGA II). *Energy Convers Manag* 2021; 236: 114065. https://doi.org/10.1016/j.enconman.2021.114065
55. Waila VC, Sharma A, Singh V, et al. Solar photovoltaic water pump performance optimization by using response surface methodology. *Environ Prog Sustain Energy* 2023; 42: e14148. https://doi.org/10.1002/ep.14148
56. Khanlari A, Badali Y and Tuncer AD. Analysis of a spiral-formed solar air heating system with ceria nanoparticles-enhanced absorber coating. *J Build Eng* 2023; 71: 106534. https://doi.org/10.1016/j.jobe.2023.106534
57. Heydari A. Experimental analysis of hybrid dryer combined with spiral solar air heater and auxiliary heating system: energy, exergy and economic analysis. *Renew Energy* 2022; 198: 1162–1175. https://doi.org/10.1016/j.renene.2022.08.110
58. Agrawal A, Rana RS and Agrawal A. Theoretical and experimental performance evaluation of single-slope single-basin solar still with multiple V-shaped floating wicks. *Heliyon* 2019; 5: 1525. https://doi.org/10.1016/j.heliyon.2019
59. Dumka P, Jain A and Mishra DR. Energy, exergy, and economic analysis of single slope conventional solar still augmented with an ultrasonic fogger and a cotton cloth. *J Energy Storage* 2020; 30: 101541. https://doi.org/10.1016/j.est.2020.101541
60. Mahmood AJ. Experimental investigation of thermal efficiency, heat losses, and economic feasibility of glazed and

unglazed solar air heaters. *Results Eng* 2025; 27: 106004. https://doi.org/10.1016/j.rineng.2025.106004
61. Gupta D, Solanki SC and Saini JS. Thermohydraulic performance of solar air heaters with roughened absorber plates. *Solar Energy*. 1997; 61(1): 33–42.
62. Ebrahim Momin AM, Saini JS and Solanki SC. Heat transfer and friction in solar air heater duct with V-shaped rib roughness on absorber plate. *International Journal of Heat and Mass Transfer*. 2002; 45(16): 3383–3396.
63. Sahu MK and Prasad RK. Thermohydraulic performance analysis of an arc shape wire roughened solar air heater. *Renew Energy* 2017; 108: 598–614. https://doi.org/10.1016/j.renene.2017.02.075
64. Rahmat MAA, Ibrahim A, Mustaffa MUS, et al. Design and performance optimization of Hollow Semi-Stadium Fins (HSSF) at multi-level array configuration for solar air collector. *Int Commun Heat Mass Tran* 2025; 166: 109154. https://doi.org/10.1016/j.icheatmasstransfer.2025.109154
65. Brahma B, Shukla AK and Baruah DC. Energy, exergy, economic and environmental analysis of Phase Change Material Based Solar Dryer (PCMSD). *J Energy Storage* 2024; 88: 111490. https://doi.org/10.1016/j.est.2024.111490
66. Singh AP, Tiwari S and Sinhmar H. A novel photovoltaic thermal and thermoelectric converter air collector integrated with solar dryer having thermal energy storage - an experimental approach. *J Energy Storage* 2025; 108: 115115. https://doi.org/10.1016/j.est.2024.115115
67. Almeshaal M, Palaniappan M and Matheswaran MM. Assessment and enhancement of thermal performance for ring roughened finned jet impingement solar air heater for low-temperature applications. *Energy* 2024; 307: 132632. https://doi.org/10.1016/j.energy.2024.132632
68. Abdulmejeed AEA, Tuncer AD, Khanlari A, et al. Investigation of combined parallel and triple-pass v-corrugated solar air heater: a numerical and experimental study. *Process Saf Environ Prot* 2024; 185: 1385–1398. https://doi.org/10.1016/j.psep.2024.03.107
69. Sureandhar G, Srinivasan G, Muthukumar P, et al. Performance analysis of arc rib fin embedded in a solar air heater. *Therm Sci Eng Prog* 2021; 23: 100891. https://doi.org/10.1016/j.tsep.2021.100891
70. Albdoor AK, Obaid ZAH, Kamel MS, et al. Energy, exergy, economic and environmental analysis of a solar air heater integrated with double triangular fins: experimental investigation. *Int J Thermofluids* 2024; 24: 100979. https://doi.org/10.1016/j.ijft.2024.100979
71. Gogada S, Roy S, Gupta A, et al. Energy and exergy analysis of solar air heater with trapezoidal ribs based absorber: a comparative analysis. *Energy Sci Eng* 2023; 11(2): 585–605. https://doi.org/10.1002/ese3.1347

Appendix

Nomenclature

u	Velocity component in x direction (m/s)
v	Velocity component in y direction (m/s)
w	Velocity component in z direction (m/s)
P	Pressure (N/m^2)
T	Temperature (K)
S	Solar Flux (W/m^2)
U	Overall Heat transfer coefficient ($W/m^2.K$)
h	Heat transfer coefficient ($W/m^2.K$)
Nu	Nusselt Number
f	Friction Factor
V	Velocity of air (m/s)
C_P	Specific Heat (J/Kg. K)
D_e	Hydraulic Diameter (K)
p	Perimeter (m)
T_{Sun}	Sun temperature (K)
y	Inaccuracy in measurement
W	Work required by blower (Watt)
m_{air}	Mass flow rate of air (kg/s)
i	Inflation (%)
S_L	Salvage value.

Symbols

ρ	Density of Air (Kg/m^3)
ε	Emissivity of absorber plate material
k	Kinetic Energy
η_f	Efficiency of fin (%)
η_{th}	Thermal Efficiency of Solar Air Heater (%)
η_X	Exergetic efficiency of SAH (%)
β	Coefficient of volume expansion (1/K)
φ	Viscous heat dissipation

Acronyms

SAH	Solar Air Heater
TFSAH	Triangular Fins Solar Air Heater
TFSAHN	Triangular Fins Solar Air Heater Numerical
TFSAHE	Triangular Fins Solar Air Heater Experimental
TFSAHR	Triangular Fins Solar Air Heater with Ribs
TFSAHRN	Triangular Fins Solar Air Heater with Ribs Numerical
TFSAHRE	Triangular Fins Solar Air Heater with Ribs Experimental
FF	Friction Factor
TPF	Thermal Performance Factor
PD	Pressure Drop
HT	Heat Transfer
AC	Annual Cost
TC	Total Cost
AMC	Annual Maintenance Cost
CFD	Computational Fluid Dynamics
ASV	Annual Salvage Value
APC	Annual Power Cost
MFR	Mass flow Rate
EE	Exergy Efficiency.